*J. Fluid Mech.* (2016), *vol.* 791, *pp.* 122–153.  
doi:10.1017/jfm.2016.42

# Drag reduction in a thermally modulated channel

**M. Z. Hossain**[1,†] **and J. M. Floryan**[1]

[1]Department of Mechanical and Materials Engineering, The University of Western Ontario, London, Ontario, N6A 5B9, Canada

(Received 15 July 2015; revised 30 December 2015; accepted 10 January 2016; first published online 15 February 2016)

Flow in a horizontal channel exposed to external heating which results in sinusoidal temperature variations along the upper and lower walls with a phase shift between them has been studied using a combination of analytical and numerical methods. The most intense convection is observed when the upper and lower hot spots are located above each other. It has been demonstrated that the heating results in a significant reduction of the pressure gradient required to drive the flow when compared to a similar flow in an isothermal channel. The drag reduction is associated with the formation of separation bubbles which insulate the stream from direct contact with the bounding walls. The fluid inside of the bubbles rotates due to horizontal density gradients, which further reduces the required pressure gradient. The magnitude of the drag reduction depends on the phase shift between the heating patterns and can increase by up to threefold when compared to the drag reduction which can be achieved by heating only one wall. A detailed analysis of the associated heat fluxes has been presented.

**Key words:** convection, drag reduction, flow control

## 1. Introduction

The search for drag reduction has been one of the main interests of fluid mechanics for at least the last hundred years. The overall drag may consist of pressure form drag, pressure interaction drag and shear drag (Mohammadi & Floryan 2012). The first type of drag results from the pressure field asymmetry between the upstream and downstream sides of a moving object and techniques for its reduction are well understood. The second type of drag results from the projection of the pressure field onto the surface topography and its understanding is limited. The third type of drag results from the friction between the fluid and the bounding solid wall and the development of techniques for its reduction have attracted a lot of interest in recent years. The present analysis contributes to these efforts.

The magnitude of the frictional drag depends on the fluid viscosity and velocity gradients at the wall. Assuming that the fluid type cannot be altered, one needs to develop techniques for altering the character of the fluid motion in the vicinity of the

†Email address for correspondence: mhossa7@uwo.ca

bounding solid surface. The most explored route involves the control of the laminar–turbulent transition as the laminar shear stress is much smaller than the turbulent shear stress. Assuming that the type of flow cannot be changed, one can seek methods for the rearrangement of the velocity field in the vicinity of the solid wall, i.e. generating new forms of either laminar or turbulent flows with the hope that they will produce less friction. The desired changes can be created using either passive or active means. The wall topography, application of suction/blowing and/or use of plasma-, sound- or piezo-driven actuators represent commonly used techniques. New ideas are sought from biological systems as natural evolution must have led to the optimization of their performance (Martin & Bhushan 2014).

Reduction of the laminar shear drag is the focus of the present work. One way to achieve this goal is through the development of the proper surface topography. If one takes the smooth surface as the reference case, all its alterations will increase the wetted area and thus the reduction of the wall shear stress must be large enough to overcome the potential drag increase due to the increase of surface area exposed to the shear stress. It is known that longitudinal grooves (grooves parallel to the flow direction) can lead to a significant drag reduction through changes in the distribution of the bulk flow (Mohammadi & Floryan 2013*a*, 2014, 2015; Moradi & Floryan 2013). The groove shapes can be optimized (Mohammadi & Floryan 2013*b*) with the optimal shape having a universal form which depends on the constraints used. In the case of grooves with equal height and depth, the universal form has a trapezoidal shape, while in the case of grooves with different depth and height it has a Gaussian shape. The grooves are effective if the flow remains laminar and the required estimates of the stability limits are available (Moradi & Floryan 2014).

The second group of techniques relies on the superhydrophobic effect (Rothstein 2010). The surface topography traps gas bubbles in micropores, replacing the shear stress between the liquid and the solid with a shear stress between the liquid and the gas. This effect is active in two-phase systems and its effectiveness depends on the hydrophobicity of the liquid–solid system and details of the surface topography. Laminar drag reduction has been demonstrated by Ou, Perot & Rothstein (2004), Ou & Rothstein (2005), Joseph *et al.* (2006) and Truesdell *et al.* (2006), among others. The effectiveness of this method can be increased by correctly shaping the surface pores (Samaha, Tafreshi & Gad-el-Hak 2011) and by increasing hydrophobicity through changes in the surface chemistry (Quéré 2008; Reyssat, Yeomans & Quéré 2008; Zhou *et al.* 2011). While the reduction of the shear stress is obvious, the pressure drag must counteract it but nevertheless, the system exhibits an overall drag reduction as demonstrated experimentally. The stability characteristics of flows over such rough surfaces are yet to be established, including conditions which guarantee the existence of a laminar flow.

The third group of methods relies on the use of spatial heating patterns which create a buoyancy field leading to the formation of a system of separation bubbles. The fluid trapped inside of the bubbles rotates due to the actions of horizontal density gradients and thus provides a propulsive force which contributes to the fluid pumping. The bubbles also isolate the stream from direct contact with the bounding walls and thus reduce the friction acting on the stream. This effect, sometimes referred to as the superthermohydrophobic effect (Floryan 2012), operates in single-phase fluids and is independent of the surface topography and thus offers advantages over the superhydrophobic effect. Its heat transfer consequences have been discussed in Hossain & Floryan (2013*a*). The strength is increased by combining the spatially distributed heating and the uniform heating of the lower wall

(Floryan & Floryan 2015). The effect is resilient as it can be generated by heating applied either at the lower or at the upper wall (Hossain & Floryan 2014). The flow must remain laminar for the method to work but stability characteristics, which can be inferred from the analysis of channel flow exposed to a spatially distributed heating at the lower wall (Hossain & Floryan 2015*a*), suggest that stability limits do not prevent applications of this effect. Its weakness is associated with the fact that it remains effective for very small Reynolds numbers (Hossain, Floryan & Floryan 2012) since stronger flows wash the separation bubbles away. This justifies the search for heating patterns which could increase the range of Reynolds numbers where the effect remains of practical value, as well as methods for increasing its strength. Yamamoto, Hasegawa & Kasagi (2013) achieved simultaneous drag reduction and heat transfer enhancement in turbulent flow using wall waves of suction/blowing travelling in the downstream direction and this demonstrates the drag reducing potential associated with non-isothermal walls. The effect subject to the present investigation is simpler due to its passive character as the heating does not depend on time.

The main objective of this analysis is to study the system response when both walls of a horizontal channel are heated and to determine the positioning of the heating patterns which lead to the largest drag reduction. A model problem and the relevant formulation are discussed in § 2. The solution method is described in § 3. The long heating wavelength solution is presented in § 4. Results for arbitrary heating wavenumbers are discussed in § 5. Section 6 provides a short summary of the main conclusions. All results presented in the discussion have been obtained for the Prandtl number $Pr = 0.71$.

## 2. Problem formulation

Consider the steady, two-dimensional flow of a fluid confined in a channel bounded by two parallel walls extending to $\pm\infty$ in the $x$-direction and placed a distance $2h$ apart from each other with the gravitational acceleration $g$ acting in the negative $y$-direction, as shown in figure 1. The flow is driven in the positive $x$-direction by a pressure gradient. The fluid is incompressible and Newtonian with thermal conductivity $k$, specific heat $c$, thermal diffusivity $\kappa = k/\rho c$, kinematic viscosity $\nu$, dynamic viscosity $\mu$, thermal expansion coefficient $\Gamma$ and variations of the density $\rho$ that follow the Boussinesq approximation. All material properties are evaluated at the mean wall temperature $T_R$ which plays the role of the reference temperature. The lower and upper walls are subjected to periodic heating patterns with a phase difference $\Omega$ between them. The resulting wall temperatures have the form

$$\theta_L(x) = \cos(\alpha x)/2, \quad \theta_U(x) = \cos(\alpha x + \Omega)/2, \tag{2.1a,b}$$

where subscripts $L$ and $U$ refer to the lower and upper walls, respectively, $\theta_L$ denotes the relative temperature of the lower wall scaled with the amplitude of its peak-to-peak variations $T_{p,L}$, i.e. $\theta_L = (T - T_R)/T_{p,L}$, $\theta_U$ denotes the relative temperature of the upper wall scaled with the amplitude of its peak-to-peak variations $T_{p,U}$, i.e. $\theta_U = (T - T_R)/T_{p,U}$, $T$ denotes the absolute temperature, $\lambda = 2\pi/\alpha$ is the wavelength of the heating and the half channel height $h$ has been used as the length scale.

The velocity and pressure fields in the absence of heating have the form

$$\boldsymbol{v}_0(x, y) = [u_0(y), 0] = [1 - y^2, 0], \quad p_0(x, y) = -2x/Re, \tag{2.2a,b}$$

where $\boldsymbol{v}_0 = (u_0, v_0)$ denotes the velocity vector scaled with the maximum of the $x$-velocity $U_{max}$, $p_0$ stands for the pressure scaled with $\rho U_{max}^2$ and the Reynolds number is defined as $Re = U_{max}h/\nu$.

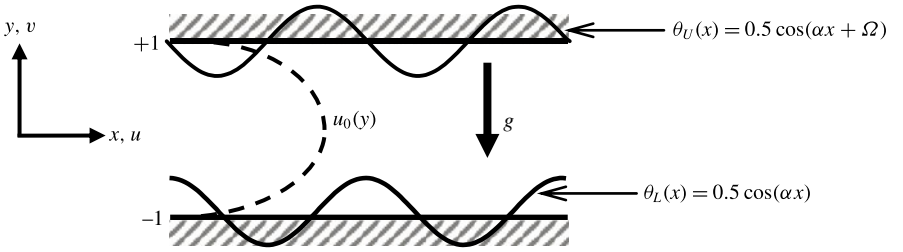


FIGURE 1. Sketch of the system configuration.

Introduction of the heating modifies the above fields, which can be represented as a superposition of the pressure-gradient-driven and the buoyancy-driven motions. The temperature field is represented as a sum of the conductive field $\theta_0$ associated with the external heating and modifications associated with the movement of the fluid. The complete flow quantities have the form

$$\left.\begin{array}{c} u_T(x,y) = Re\,u_0(y) + u_1(x,y), \quad v_T(x,y) = v_1(x,y), \\ \theta_T(x,y) = Ra_{p,L}\theta_{0,L}(x,y) + Ra_{p,U}\theta_{0,U}(x,y) + \theta_1(x,y), \quad p_T(x,y) = Re^2 p_0(x) + p_1(x,y), \end{array}\right\} \tag{2.3}$$

where $(u_T, v_T)$ denote the complete velocity vector with $(x, y)$-components, $p_T$ and $\theta_T$ denote the complete pressure and temperature fields, respectively, $(u_1, v_1)$ stands for the modification velocity vector with components in the $(x, y)$ directions, $p_1$ and $\theta_1$ denote the pressure and temperature modifications, respectively, $\theta_{0,L}$ stands for the conductive temperature field associated with the lower wall heating and $\theta_{0,U}$ stands for the conductive temperature field associated with the upper-wall heating. The complete velocity vector and the velocity modifications have been scaled using the convective velocity scale $U_v = \nu/h$ where $U_{max}/U_v = Re$, the pressure modifications have been scaled using $\rho U_v^2$ and the complete and modification temperature fields have been scaled using $\nu\kappa/(g\Gamma h^3)$ as the temperature scale. $Ra_{p,L} = g\Gamma h^3 T_{p,L}/(\nu\kappa)$ and $Ra_{p,U} = g\Gamma h^3 T_{p,U}/(\nu\kappa)$ are the lower and upper periodic Rayleigh numbers expressing the intensity of the heating applied at the respective walls.

The conductive temperature fields have the following forms

$$\theta_{0,L}(x,y) = \theta_{0,L}^{(1)}(y)\mathrm{e}^{\mathrm{i}\alpha x} + \theta_{0,L}^{(-1)}(y)\mathrm{e}^{-\mathrm{i}\alpha x},$$
$$\theta_{0,L}^{(1)}(y) = [-\sinh(\alpha y)/\sinh(\alpha) + \cosh(\alpha y)/\cosh(\alpha)]/8, \tag{2.4a}$$
$$\theta_{0,U}(x,y) = \theta_{0,U}^{(1)}(y)\mathrm{e}^{\mathrm{i}\alpha x} + \theta_{0,U}^{(-1)}(y)\mathrm{e}^{-\mathrm{i}\alpha x},$$
$$\theta_{0,U}^{(1)}(y) = \mathrm{e}^{\mathrm{i}\Omega}[\sinh(\alpha y)/\sinh(\alpha) + \cosh(\alpha y)/\cosh(\alpha)]/8, \tag{2.4b}$$

where complex notation has been used, $\theta_{0,L}^{(-1)} = \theta_{0,L}^{(1)*}$, $\theta_{0,U}^{(-1)} = \theta_{0,U}^{(1)*}$ are the additional conditions which guarantee that $\theta_{0,L}$ and $\theta_{0,U}$ are real and stars denote the complex conjugates. The field equations for the flow and temperature modifications are of the form

$$(Reu_0 + u_1)\frac{\partial u_1}{\partial x} + Rev_1\frac{\mathrm{d}u_0}{\mathrm{d}y} + v_1\frac{\partial u_1}{\partial y} = -\frac{\partial p_1}{\partial x} + \nabla^2 u_1, \tag{2.5a}$$

$$(Re\,u_0 + u_1)\frac{\partial v_1}{\partial x} + v_1\frac{\partial v_1}{\partial y} = -\frac{\partial p_1}{\partial y} + \nabla^2 v_1 + Pr^{-1}\theta_1 + Ra_{p,L}Pr^{-1}\theta_{0,L} + Ra_{p,U}Pr^{-1}\theta_{0,U}, \tag{2.5b}$$

$$(Re\,u_0+u_1)\left(Ra_{p,L}\frac{\partial\theta_{0,L}}{\partial x}+Ra_{p,U}\frac{\partial\theta_{0,U}}{\partial x}+\frac{\partial\theta_1}{\partial x}\right)$$
$$+v_1\left(Ra_{p,L}\frac{\partial\theta_{0,L}}{\partial y}+Ra_{p,U}\frac{\partial\theta_{0,U}}{\partial y}+\frac{\partial\theta_1}{\partial y}\right)=Pr^{-1}\nabla^2\theta_1, \tag{2.5c}$$

$$\frac{\partial u_1}{\partial x}+\frac{\partial v_1}{\partial y}=0, \tag{2.5d}$$

where $\nabla^2$ denotes the Laplace operator. The effects of the heating on the pressure losses are sought. The problem is posed as the question of finding the additional pressure gradient which is required in order to maintain the same flow rate in the heated and isothermal channels. This requirement is imposed in the form of the flow rate constraint, i.e.

$$Q=\int_{-1}^{1}u_T\,\mathrm{d}y=\int_{-1}^{1}(Re\,u_0+u_1)\,\mathrm{d}y=4Re/3. \tag{2.6}$$

The problem formulation is closed by specifying no slip, no penetration and the thermal boundary conditions in the form

$$u_1(\pm1)=0,\quad v_1(\pm1)=0,\quad \theta_1(\pm1)=0. \tag{2.7a–c}$$

One may consider flow in a channel heated by heat fluxes imposed at the walls which is easier to achieve experimentally. The overall system response is expected to be qualitatively similar to that achieved using the fixed wall temperatures while quantitative differences require detailed analysis.

## 3. Method of solution

The solution method is explained in detail in Hossain *et al.* (2012) and thus the following presentation is limited to a short outline. We define the stream function $\psi(x, y)$ in the usual manner, i.e. $u_1=\partial\psi/\partial y$, $v_1=-\partial\psi/\partial x$ and eliminate pressure bringing the governing equations to the form

$$Re\,u_0\frac{\partial}{\partial x}\left(\nabla^2\psi\right)-Re\frac{\mathrm{d}^2u_0}{\mathrm{d}y^2}\frac{\partial\psi}{\partial x}+N_\psi$$
$$=\nabla^4\psi-Pr^{-1}\frac{\partial\theta_1}{\partial x}-Ra_{p,L}Pr^{-1}\frac{\partial\theta_{0,L}}{\partial x}-Ra_{p,U}Pr^{-1}\frac{\partial\theta_{0,U}}{\partial x}, \tag{3.1a}$$

$$Re\,u_0\left(Ra_{p,L}\frac{\partial\theta_{0,L}}{\partial x}+Ra_{p,U}\frac{\partial\theta_{0,U}}{\partial x}+\frac{\partial\theta_1}{\partial x}\right)+Ra_{p,L}N_{\theta0,L}+Ra_{p,U}N_{\theta0,U}+N_{\theta1}=Pr^{-1}\nabla^2\theta_1, \tag{3.1b}$$

where $\nabla^4$ denotes the biharmonic operator, the nonlinear terms are written in the conservative form, i.e.,

$$N_\psi=\frac{\partial}{\partial y}\left(\frac{\partial}{\partial x}\langle u_1u_1\rangle+\frac{\partial}{\partial y}\langle u_1v_1\rangle\right)-\frac{\partial}{\partial x}\left(\frac{\partial}{\partial x}\langle u_1v_1\rangle+\frac{\partial}{\partial y}\langle v_1v_1\rangle\right), \tag{3.2}$$

$$\left.\begin{aligned} N_{\theta 1} &= \frac{\partial}{\partial x}\left\langle u_1\theta_1\right\rangle + \frac{\partial}{\partial y}\left\langle v_1\theta_1\right\rangle, \\ N_{\theta 0,L} &= \frac{\partial}{\partial x}\left\langle u_1\theta_{0,L}\right\rangle + \frac{\partial}{\partial y}\left\langle v_1\theta_{0,L}\right\rangle, \\ N_{\theta 0,U} &= \frac{\partial}{\partial x}\left\langle u_1\theta_{0,U}\right\rangle + \frac{\partial}{\partial y}\left\langle v_1\theta_{0,U}\right\rangle \end{aligned}\right\} \tag{3.3}$$

and $\langle\cdots\rangle$ denotes products. The solution is assumed to be in the form of Fourier expansions

$$\psi(x,y) = \sum_{n=-\infty}^{n=+\infty} \varphi^{(n)}(y)\mathrm{e}^{\mathrm{i}n\alpha x}, \quad \theta_1(x,y) = \sum_{n=-\infty}^{n=+\infty} \phi^{(n)}(y)\mathrm{e}^{\mathrm{i}n\alpha x}, \tag{3.4a,b}$$

$$\left.\begin{aligned} u_1(x,y) &= \sum_{n=-\infty}^{n=+\infty} u_1^{(n)}(y)\mathrm{e}^{\mathrm{i}n\alpha x}, \quad v_1(x,y) = \sum_{n=-\infty}^{n=+\infty} v_1^{(n)}(y)\mathrm{e}^{\mathrm{i}n\alpha x}, \\ p_1(x,y) &= Ax + \sum_{n=-\infty}^{n=+\infty} p_1^{(n)}(y)\mathrm{e}^{\mathrm{i}n\alpha x}, \end{aligned}\right\} \tag{3.5}$$

where $D = \mathrm{d}/\mathrm{d}y$, $u_1^{(n)} = D\varphi^{(n)}$, $v_1^{(n)} = -\mathrm{i}n\alpha\varphi^{(n)}$, $\varphi^{(n)} = \varphi^{(-n)*}$, $\phi^{(n)} = \phi^{(-n)*}$, $u_1^{(n)} = u_1^{(-n)*}$, $v_1^{(n)} = v_1^{(-n)*}$, $p_1^{(n)} = p_1^{(-n)*}$ and $A$ stands for the streamwise pressure gradient correction induced by the heating. Positive values of $A$ correspond to drag reduction. The products are expressed using Fourier expansions of the form

$$\langle FG\rangle = \sum_{n=-\infty}^{n=+\infty} \langle FG\rangle^{(n)}(y)\mathrm{e}^{\mathrm{i}n\alpha x}, \tag{3.6}$$

where $\langle FG\rangle$ stands for any of the following quantities: $\langle u_1u_1\rangle$, $\langle u_1v_1\rangle$, $\langle v_1v_1\rangle$, $\langle u_1\theta_1\rangle$, $\langle v_1\theta_1\rangle$, $\langle u_1\theta_{0,L}\rangle$, $\langle v_1\theta_{0,L}\rangle$, $\langle u_1\theta_{0,U}\rangle$, $\langle v_1\theta_{0,U}\rangle$. Substitution of (3.4)–(3.6) into (3.1) and separation of Fourier components result in a system of ordinary differential equations for the modal functions of the form

$$\begin{aligned} D_n^2\varphi^{(n)} - \mathrm{i}n\alpha\, Re(u_0D_n - D^2u_0)\varphi^{(n)} - \mathrm{i}n\alpha\, Pr^{-1}\phi^{(n)} \\ = \mathrm{i}n\alpha\, Ra_{p,L}\, Pr^{-1}\theta_{0,L}^{(n)} + \mathrm{i}n\alpha\, Ra_{p,U}\, Pr^{-1}\theta_{0,U}^{(n)} + N_\psi^{(n)}, \end{aligned} \tag{3.7}$$

$$\begin{aligned} D_n\phi^{(n)} - \mathrm{i}n\alpha\, Pr\, Re\, u_0\phi^{(n)} = \mathrm{i}n\alpha\, PrRe\, u_0\,(Ra_{p,L}\theta_{0,L}^{(n)} + Ra_{p,U}\theta_{0,U}^{(n)}) \\ + PrRa_{p,L}N_{\theta 0,L}^{(n)} + PrRa_{p,U}N_{\theta 0,U}^{(n)} + Pr\,N_{\theta 1}^{(n)}, \end{aligned} \tag{3.8}$$

where

$$\left.\begin{aligned} D^2 = \mathrm{d}^2/\mathrm{d}y^2, \quad D_n = D^2 - n^2\alpha^2, \quad N_{\theta 0,L}^{(n)} &= \mathrm{i}n\alpha\langle u_1\theta_{0,L}\rangle^{(n)} + D\langle v_1\theta_{0,L}\rangle^{(n)}, \\ N_{\theta 1}^{(n)} &= \mathrm{i}n\alpha\langle u_1\theta_1\rangle^{(n)} + D\langle v_1\theta_1\rangle^{(n)}, \\ N_\psi^{(n)} &= \mathrm{i}n\alpha D\langle u_1u_1\rangle^{(n)} + D^2\langle u_1v_1\rangle^{(n)} + n^2\alpha^2\langle u_1v_1\rangle^{(n)} - \mathrm{i}n\alpha D\langle v_1v_1\rangle^{(n)}, \\ -\infty < n < \infty. \end{aligned}\right\} \tag{3.9}$$

The reader may note that $\theta_{0,L}^{(n)} = 0$ and $\theta_{0,U}^{(n)} = 0$ for $n \neq \pm 1$. The required boundary conditions for the modal functions have the form

$$D\varphi^{(n)}(\pm 1) = 0, \quad \varphi^{(n)}(\pm 1) = 0, \quad \phi^{(n)}(\pm 1) = 0. \tag{3.10a–c}$$

The system (3.7), (3.8) and (3.10) needs to be solved numerically.

For the purpose of numerical solution, expansions (3.4)–(3.6) have been truncated after $N_M$ terms. The $y$-discretization uses the Chebyshev collocation technique based on $N_T$ collocation points (Canuto *et al.* 2006). The resulting nonlinear algebraic system of equations is solved using an iterative technique combined with under-relaxation of the form $\Phi_{j+1} = \Phi_j + \varpi(\Phi_{comp} - \Phi_j)$ where $\Phi = \{\varphi^{(n)}, \phi^{(n)}\}$ is the vector of unknowns, $\Phi_{comp}$ denotes the current solution, $\Phi_j$ denotes the previous solution, $\Phi_{j+1}$ stands for the accepted value of the next iteration and $\varpi$ denotes the relaxation factor. The solution process starts with solving (3.7), (3.8) with the nonlinear terms on the right-hand side assumed to be zero, the first approximation of the nonlinear terms is computed on the basis of the available approximation of the velocity and temperature fields and the system (3.7), (3.8) is solved with the new approximation of the nonlinear terms used on the right-hand side, resulting in the first-order fixed point method. The iteration process is continued until the convergence criterion $\max(|\Phi_{comp} - \Phi_j|) < \mathrm{TOL}$ is satisfied where TOL denotes the specified error. The number of iterations is varied by several orders of magnitude depending on the flow parameters; there was no attempt to optimize the relaxation factor $\varpi$. The number of collocation points and the number of Fourier modes used in the solution were selected through systematic numerical tests so that the quantities of interest were determined with at least six digits accuracy. Typically $N_T = 50$ provided sufficient accuracy. The required value of $N_M$ strongly depends on $\alpha$, $Re$, $Ra_{p,U}$ and $Ra_{p,L}$, and can be as large as $N_M = 50$.

The evaluation of the nonlinear terms requires the evaluation of products of two Fourier series. The required quantities were computed in the physical space on a suitable grid based on the collocation points in the $y$-direction and a uniformly distributed set of points in the $x$-direction, the relevant products were evaluated on this grid and the fast Fourier transform (FFT) algorithm was used to express these products in terms of Fourier expansions (3.6). The aliasing error was controlled using the discrete FFT transform with $N_E$ rather than $N_M$ points, where $N_E \geqslant 3N_M/2$ (Canuto *et al.* 2006).

The pressure field has been computed *a posteriori* from the $x$-momentum equation. Insertion of (3.4)–(3.6) into (2.5*a*) and separation of Fourier modes lead to

$$p_1^{(n)} = \frac{1}{\mathrm{i}n\alpha}\left[(D^2 - n^2\alpha^2 - \mathrm{i}n\alpha\, Re\, u_0)\, D\varphi^{(n)} + \mathrm{i}n\alpha\, Re \frac{\mathrm{d}u_0}{\mathrm{d}y}\varphi^{(n)} - \mathrm{i}n\alpha\, \langle u_1 u_1\rangle^{(n)} - D\langle u_1 v_1\rangle^{(n)}\right] \quad \text{for } n \neq 0, \tag{3.11}$$

$$A = D^3\varphi^{(0)} - D\,\langle u_1 v_1\rangle^{(0)} \quad \text{for } n = 0. \tag{3.12}$$

Equation (3.12) provides a means for the evaluation of the additional pressure gradient $A$ required to maintain the same flow rates in the heated and unheated channels. Equation (3.11) has been used to compute $p_1^{(n)}$, $n \neq 0$. One needs to use the $y$-momentum (2.5*b*) for the determination of $p_1^{(0)}$. Substitution of (3.4)–(3.6) into (2.5*b*), extraction of mode zero and integration result in

$$p_1^{(0)} = Pr^{-1}\int_{-1}^{y}\varphi^{(0)}\mathrm{d}y - \langle v_1 v_1\rangle^{(0)} + Ra_{p,L}Pr^{-1}\int_{-1}^{y}\theta_{0,L}^{(0)}\,\mathrm{d}y + Ra_{p,U}Pr^{-1}\int_{-1}^{y}\theta_{0,U}^{(0)}\,\mathrm{d}y. \tag{3.13}$$

The wall shear stresses acting on the fluid at the upper ($\tau_U$) and lower ($\tau_L$) walls are of interest as they are responsible for the drag generation. They can be expressed as

$$\tau_U = \left.\frac{\partial u_1}{\partial y}\right|_{y=1} - 2Re, \quad \tau_L = -\left.\frac{\partial u_1}{\partial y}\right|_{y=-1} - 2Re \tag{3.14a,b}$$

and their average values can be evaluated as

$$\tau_{U,ave} = \left.\frac{\mathrm{d}^2\varphi^{(0)}}{\mathrm{d}y^2}\right|_{y=1} - 2Re = \tau_{U,mod} - 2Re, \quad \tau_{L,ave} = -\left.\frac{\mathrm{d}^2\varphi^{(0)}}{\mathrm{d}y^2}\right|_{y=-1} - 2Re = \tau_{L,mod} - 2Re, \tag{3.15a,b}$$

where $\tau_{U,mod}$ and $\tau_{L,mod}$ stand for upper and lower wall shear stress modifications due to the heating, respectively. Changes in the shear stress result in changes in the pressure gradient, e.g.

$$\left.\frac{\partial p_T}{\partial x}\right|_{mean} = Re(-2 + A/Re), \quad \tau_{U,mod} + \tau_{L,mod} = 2A, \tag{3.16a,b}$$

with the effectiveness of the heating judged by comparing $A$ with the isothermal pressure gradient $-2Re$ (or by comparing $A/Re$ with $-2$). Relation (3.16*b*) can be easily derived by looking at the force balance on a convenient control volume. The heat fluxes leaving the walls are expressed in terms of the Nusselt numbers defined as

$$\left.\begin{aligned} Nu_U &= Ra_{p,L}\left.\frac{\mathrm{d}\theta_{0,L}}{\mathrm{d}y}\right|_{y=1} + Ra_{p,U}\left.\frac{\mathrm{d}\theta_{0,U}}{\mathrm{d}y}\right|_{y=1} + \left.\frac{\mathrm{d}\theta_1}{\mathrm{d}y}\right|_{y=1}, \\ Nu_L &= -Ra_{p,L}\left.\frac{\mathrm{d}\theta_{0,L}}{\mathrm{d}y}\right|_{y=-1} - Ra_{p,L}\left.\frac{\mathrm{d}\theta_{0,U}}{\mathrm{d}y}\right|_{y=-1} - \left.\frac{\mathrm{d}\theta_1}{\mathrm{d}y}\right|_{y=-1}. \end{aligned}\right\} \tag{3.17}$$

The net heat flux between the walls is expressed in term of the average Nusselt number of the form

$$Nu_{av} = Nu_{av,L} = Nu_{av,U} = \frac{1}{\lambda}\int_0^{\lambda}\left(-\left.\frac{\mathrm{d}\theta_T}{\mathrm{d}y}\right|_{y=-1}\right)\mathrm{d}x = -\left.\frac{\mathrm{d}\phi^{(0)}}{\mathrm{d}y}\right|_{y=-1} \tag{3.18}$$

and the horizontal heat fluxes along each wall can be measured in terms of the periodic part of the heat flux leaving the heated segment of each wall. These fluxes can be expressed in terms of the horizontal Nusselt numbers for the lower ($Nu_{h,L}$) and upper ($Nu_{h,U}$) walls defined as

$$\left.\begin{aligned} Nu_{h,L} &= \frac{2}{\lambda}\int_{-\lambda/4}^{\lambda/4}\left(-\left.\frac{\partial\theta_T}{\partial y} + \frac{\mathrm{d}\phi^{(0)}}{\mathrm{d}y}\right)\right|_{y=-1}\mathrm{d}x, \\ Nu_{h,U} &= \frac{2}{\lambda}\int_{-\lambda/4-\Omega/\alpha}^{\lambda/4-\Omega/\alpha}\left(\left.\frac{\partial\theta_T}{\partial y} - \frac{\mathrm{d}\phi^{(0)}}{\mathrm{d}y}\right)\right|_{y=1}\mathrm{d}x. \end{aligned}\right\} \tag{3.19}$$

Alternative methods to determine horizontal fluxes can be found in Maxworthy (1997), Siggers, Kerswell & Balmforth (2004), Hughes & Griffiths (2008) and Winters & Young (2009).

We shall start the analysis with the long wavelength heating as this case can be solved analytically and thus provides useful insight into the flow dynamics.

## 4. Long wavelength heating

The conductive temperature field (2.4) can be approximated as

$$\theta_{0,L}(x,y) = [\theta_{L0}(y) + \alpha^2\theta_{L2}(y) + \alpha^4\theta_{L4}(y) + O(\alpha^6)]\cos X, \tag{4.1a}$$

$$\theta_{0,U}(x,y) = [\theta_{U0}(y) + \alpha^2\theta_{U2}(y) + \alpha^4\theta_{U4}(y) + O(\alpha^6)]\cos(X+\Omega), \tag{4.1b}$$

where definitions of the expansion coefficients are given in appendix A and $X = \alpha x$ denotes the slow scale. The field equations with $x$ replaced by the slow scale assume the form

$$\alpha\,(Re\,u_0 + u_1)\,\frac{\partial u_1}{\partial X} + Re\,v_1\frac{\mathrm{d}u_0}{\mathrm{d}y} + v_1\frac{\partial u_1}{\partial y} = -\alpha\frac{\partial p_1}{\partial X} + \alpha^2\frac{\partial^2 u_1}{\partial X^2} + \frac{\partial^2 u_1}{\partial y^2}, \tag{4.2a}$$

$$\alpha(Re\,u_0 + u_1)\frac{\partial v_1}{\partial X} + v_1\frac{\partial v_1}{\partial y} = -\frac{\partial p_1}{\partial y} + \alpha^2\frac{\partial^2 v_1}{\partial X^2} + \frac{\partial^2 v_1}{\partial y^2} + Pr^{-1}\theta_1 + Ra_{p,L}Pr^{-1}\theta_{0,L} + Ra_{p,U}Pr^{-1}\theta_{0,U}, \tag{4.2b}$$

$$\alpha(Re\,u_0 + u_1)\left(Ra_{p,L}\frac{\partial\theta_{0,L}}{\partial X} + Ra_{p,U}\frac{\partial\theta_{0,U}}{\partial X} + \frac{\partial\theta_1}{\partial X}\right) + v_1\left(Ra_{p,L}\frac{\partial\theta_{0,L}}{\partial y} + Ra_{p,U}\frac{\partial\theta_{0,U}}{\partial y} + \frac{\partial\theta_1}{\partial y}\right) = Pr^{-1}\left(\alpha^2\frac{\partial^2\theta_1}{\partial X^2} + \frac{\partial^2\theta_1}{\partial y^2}\right), \tag{4.2c}$$

$$\alpha\frac{\partial u_1}{\partial X} + \frac{\partial v_1}{\partial y} = 0. \tag{4.2d}$$

Their solution can be represented as

$$\left.\begin{aligned}[u_1(X,y),\,v_1(X,y),\,\theta_1(X,y)] &= \sum_{n=1}^{4}\alpha^n[U_n(X,y),\,V_n(X,y),\,\Theta_n(X,y)] + O(\alpha^5),\\ p_1(X,y) &= \sum_{n=0}^{3}\alpha^n P_n(X,y) + O(\alpha^4).\end{aligned}\right\} \tag{4.3}$$

Expansions (4.1) and (4.3) are substituted into (4.2) and terms of the same order of magnitude are separated. System $O(\alpha)$ has the form

$$\left.\begin{aligned}&\frac{\partial P_0}{\partial y} = Ra_{p,L}Pr^{-1}\theta_{L0}\cos X + Ra_{p,U}Pr^{-1}\theta_{U0}\cos(X+\Omega),\\ &\frac{\partial^2\Theta_1}{\partial y^2} = -Reu_0Pr\,\left[Ra_{p,L}\theta_{L0}\sin X + Ra_{p,U}\theta_{U0}\sin(X+\Omega)\right],\quad \frac{\partial^2 U_1}{\partial y^2} = \frac{\partial P_0}{\partial X},\\ &\frac{\partial U_1}{\partial X} + \frac{\partial V_2}{\partial y} = 0,\quad U_1(\pm1) = V_1(\pm1) = \Theta_1(\pm1) = 0,\quad \int_{-1}^{1}U_1\,\mathrm{d}y = 0\end{aligned}\right\} \tag{4.4}$$

and its solution can be expressed as

$$U_1(X,y) = Pr^{-1}[Ra_{p,L}F_{U11}(y)\sin X + Ra_{p,U}F_{U12}(y)\sin(X+\Omega)], \tag{4.5a}$$

$$V_2(X,y) = Pr^{-1}[\,Ra_{p,L}F_{V21}(y)\cos X + Ra_{p,U}F_{v22}(y)\cos(X+\Omega)], \tag{4.5b}$$

$$P_0(X, y) = Pr^{-1}[Ra_{p,L}F_{P01}(y)\cos X + Ra_{p,U}F_{P02}(y)\cos(X+\Omega)], \quad (4.5c)$$

$$\Theta_1(X, y) = Re\,Pr[Ra_{p,L}F_{\Theta 11}(y)\sin X + Ra_{p,U}F_{\Theta 12}(y)\sin(X+\Omega)], \quad (4.5d)$$

with definitions of $F_{U11}$, $F_{U12}$, $F_{V21}$, $F_{V22}$, $F_{P01}$, $F_{P02}$, $F_{\Theta 11}$, $F_{\Theta 12}$ given in appendix A. $U_1$, $V_2$ and $P_0$ represent the natural convection which is unaffected by the forced convection at this level of approximation, and $\Theta_1$ represents modifications of the temperature field generated by the forced convection. The heating is unable to affect the mean streamwise pressure gradient and, since the temperature field defined by (4.5*d*) is purely periodic, there is no net heat transfer between the walls. The next-order system has the form

$$\frac{\partial^2 U_2}{\partial y^2} = \frac{\partial P_1}{\partial X} + Re\left(u_0\frac{\partial U_1}{\partial X} + \frac{\mathrm{d}u_0}{\mathrm{d}y}V_2\right), \quad \frac{\partial P_1}{\partial y} = Pr^{-1}\Theta_1, \quad \frac{\partial U_2}{\partial X} + \frac{\partial V_3}{\partial y} = 0 \quad (4.6a\text{–}c)$$

$$\begin{aligned}\frac{\partial^2 \Theta_2}{\partial y^2} &= Re\,u_0 Pr\frac{\partial \Theta_1}{\partial X} - PrU_1[Ra_{p,L}\theta_{L0}\sin X + Ra_{p,U}\theta_{U0}\sin(X+\Omega)] \\ &\quad + Pr\,V_2\left[Ra_{p,L}\frac{\partial \theta_{L0}}{\partial y}\cos X + Ra_{p,U}\frac{\partial \theta_{U0}}{\partial y}\cos(X+\Omega)\right]. \quad (4.6d)\end{aligned}$$

A similar solution procedure leads to

$$\begin{aligned}U_2(X, y) &= Re\,[Ra_{p,L}\{F_{U21}(y) + Pr^{-1}F_{U22}(y)\}\cos X \\ &\quad + Ra_{p,U}\{F_{U23}(y) + Pr^{-1}F_{U24}(y)\}\cos(X+\Omega)], \quad (4.7a)\\ V_3(X, y) &= Re\,[Ra_{p,L}\{F_{V31}(y) + Pr^{-1}F_{V32}(y)\}\sin X \\ &\quad + Ra_{p,U}\{F_{V33}(y) + Pr^{-1}F_{V34}(y)\}\sin(X+\Omega)], \quad (4.7b)\\ P_1(X, y) &= Re\,[Ra_{p,L}\{F_{P11}(y) - \tfrac{1}{1050}Pr^{-1}\}\sin X \\ &\quad + Ra_{p,U}\{F_{P12}(y) + \tfrac{1}{1050}Pr^{-1}\}\sin(X+\Omega)], \quad (4.7c)\\ \Theta_2(X, y) &= Ra_{p,L}^2F_{\Theta 21}(y) + Ra_{p,L}Ra_{p,U}F_{\Theta 22}(y)\cos\Omega + Ra_{p,U}^2F_{\Theta 23}(y) \\ &\quad + Re^2Pr^2[Ra_{p,L}F_{\Theta 24}(y)\cos X + Ra_{p,U}F_{\Theta 25}(y)\cos(X+\Omega)] \\ &\quad + Ra_{p,L}^2F_{\Theta 26}(y)\cos(2X) + Ra_{p,L}Ra_{p,U}F_{\Theta 27}(y)\cos(2X+\Omega) \\ &\quad + Ra_{p,U}^2F_{\Theta 28}(y)\cos(2X+2\Omega), \quad (4.7d)\end{aligned}$$

with definitions of $F_{U21}$–$F_{U24}$, $F_{V31}$–$F_{V34}$, $F_{P11}$–$F_{P12}$, $F_{\Theta 21}$–$F_{\Theta 28}$ given in appendix A. The temperature field defined by (4.7*d*) contains an aperiodic part (the first three terms) which describes the net heat transfer between the walls and the corresponding average Nusselt number has the form

$$Nu_{av} = \left[\tfrac{1}{1400}(Ra_{p,L}^2 + Ra_{p,U}^2) + \tfrac{17}{12\,600}Ra_{p,L}Ra_{p,U}\cos\Omega\right]\alpha^2 + O(\alpha^4). \quad (4.8)$$

The pressure field contains only $x$-periodic terms and thus the heating is unable to generate any change in the pressure gradient. The next-order system has the form

$$\frac{\partial^2 U_3}{\partial y^2} = \frac{\partial P_2}{\partial X} + Re\left(u_0\frac{\partial U_2}{\partial X} + \frac{\mathrm{d}u_0}{\mathrm{d}y}V_3\right) + U_1\frac{\partial U_1}{\partial X} + V_2\frac{\partial U_1}{\partial y} - \frac{\partial^2 U_1}{\partial X^2}, \quad (4.9a)$$

$$\frac{\partial P_2}{\partial y} = \frac{\partial^2 V_2}{\partial y^2} + Pr^{-1}\Theta_2 + Pr^{-1}\left[Ra_{p,L}\theta_{L2}\cos X + Ra_{p,U}\theta_{U2}\cos(X+\Omega)\right], \quad (4.9b)$$

$$\frac{\partial U_3}{\partial X}+\frac{\partial V_4}{\partial y}=0, \tag{4.9c}$$

$$\begin{aligned}\frac{\partial^2\Theta_3}{\partial y^2}=&\,Re\,u_0Pr\frac{\partial\Theta_2}{\partial X}-Reu_0Pr\left[Ra_{p,L}\theta_{L2}\sin X+Ra_{p,U}\theta_{U2}\sin(X+\Omega)\right]+PrU_1\frac{\partial\Theta_1}{\partial X}\\&-PrU_2\left[Ra_{p,L}\theta_{L0}\sin X+Ra_{p,U}\theta_{U0}\sin(X+\Omega)\right]+PrV_2\frac{\partial\Theta_1}{\partial y}\\&+Pr\,V_3\left[Ra_{p,L}\frac{\partial\theta_{L0}}{\partial y}\cos X+Ra_{p,U}\frac{\partial\theta_{U0}}{\partial y}\cos(X+\Omega)\right]-\frac{\partial^2\Theta_1}{\partial X^2}.\end{aligned} \tag{4.9d}$$

All forcing terms are purely periodic and thus there are no contributions to the net heat flux as well as to the pressure gradient correction.

It is sufficient to consider only the $x$-momentum equation at the next level of approximation in order to determine the pressure gradient correction, i.e.

$$\frac{\partial^2U_4}{\partial y^2}=\frac{\partial P_3}{\partial X}+Re\left(u_0\frac{\partial U_3}{\partial X}+\frac{\mathrm{d}u_0}{\mathrm{d}y}V_4\right)-\frac{\partial^2U_2}{\partial X^2}+U_1\frac{\partial U_2}{\partial X}+U_2\frac{\partial U_1}{\partial X}+V_2\frac{\partial U_2}{\partial y}+V_3\frac{\partial U_1}{\partial y}. \tag{4.10}$$

It can be shown that only the last two terms on the right-hand side of (4.10) contribute to the aperiodic forcing, and this forcing has the form

$$\begin{aligned}FF(y)=&\,\tfrac{1}{2}Re\,Pr^{-1}\left\{[Ra_{p,L}F_{V21}(y)+Ra_{p,U}F_{V22}(y)\cos\Omega]\right.\\&\times[Ra_{p,L}(DF_{U21}(y)+Pr^{-1}DF_{U22}(y))+Ra_{p,U}(DF_{U23}(y)+Pr^{-1}DF_{U24}(y))\cos\Omega]\\&+[Ra_{p,L}DF_{U11}(y)+Ra_{p,U}DF_{U12}(y)\cos\Omega]\\&\times[Ra_{p,L}(F_{V31}(y)+Pr^{-1}F_{V32}(y))+Ra_{p,U}(F_{V33}(y)+Pr^{-1}F_{V34}(y))\cos\Omega]\\&+Ra_{p,U}^2[F_{V22}(y)(DF_{U23}(y)+Pr^{-1}DF_{U24}(y))\\&\left.+(F_{V33}(y)+Pr^{-1}F_{V34}(y))\,DF_{U12}]\sin^2\Omega\right\}\end{aligned} \tag{4.11}$$

and is responsible for the pressure gradient changes. Solution of (4.11) with the appropriate boundary conditions and the flow rate constraint results in the simultaneous determination of the aperiodic part of $U_4$ and the pressure gradient correction of the form

$$U_4(y)|_{mean}=\frac{1}{2}\left.\frac{\partial p_3}{\partial X}\right|_{mean}(y^2-1)-\frac{1}{2}(y+1)\int_{-1}^{1}\int_{-1}^{y}FF(\eta)\,\mathrm{d}\eta\,\mathrm{d}y+\int_{-1}^{y}\int_{-1}^{\zeta}FF(\eta)\,\mathrm{d}\eta\,\mathrm{d}\zeta, \tag{4.12}$$

$$\left.\frac{\partial p_3}{\partial X}\right|_{mean}=-\frac{3}{2}\int_{-1}^{1}\int_{-1}^{y}FF(\eta)\,\mathrm{d}\eta\,\mathrm{d}y+\frac{3}{2}\int_{-1}^{1}\int_{-1}^{y}\int_{-1}^{\zeta}FF(\eta)\,\mathrm{d}\eta\,\mathrm{d}\zeta\,\mathrm{d}y. \tag{4.13}$$

Evaluations of the integrals result in

$$\begin{aligned}A\;=\;&\frac{\alpha^4\,Re\,Pr^{-2}}{8513\,505\,000}\left[(1929+3130\,Pr)(Ra_{p,L}^2+Ra_{p,U}^2)\right.\\&\left.+2(1896+3095\,Pr)\,Ra_{p,L}Ra_{p,U}\cos\Omega\right].\end{aligned} \tag{4.14}$$

Equation (4.14) demonstrates that the heating always reduces the pressure losses as $A$ is always positive. Use of either the lower heating only or the upper heating only results in the same drag reduction as predicted by Hossain *et al.* (2012). The maximum drag reduction for the dual heating corresponds to $\Omega = 0$ and is much larger than the drag reduction achieved with one-wall heating. It consists of separate contributions from each heating (the first term in the square bracket on the right-hand side) plus an effect resulting from the interactions between both heatings (the second term in the square bracket). The interaction term can change sign depending on $\Omega$ and it reduces the pressure gradient correction for $\pi/2 < \Omega < 3\pi/2$. The minimum of $A$ corresponds to $\Omega = \pi$ and is smaller than what can be achieved with one-wall heating. Regardless of the phase shift between the upper and the lower heating patterns, the drag reduction decreases as $\alpha^4$ when $\alpha \to 0$.

Contributions to the net heat transfer between the walls are described by the energy equation which, at this level of approximation, assumes the form

$$\begin{aligned}\frac{\partial^2\Theta_4}{\partial y^2} &= Re\,u_0 Pr\frac{\partial\Theta_3}{\partial X} - PrU_1[Ra_{p,L}\theta_{L2}\sin X + Ra_{p,U}\theta_{U2}\sin(X+\Omega)]\\ &\quad - PrU_3[Ra_{p,L}\theta_{L0}\sin X + Ra_{p,U}\theta_{U0}\sin(X+\Omega)]\\ &\quad + Pr\left[U_1\frac{\partial\Theta_2}{\partial X} + U_2\frac{\partial\Theta_1}{\partial X} + V_2\frac{\partial\Theta_2}{\partial y} + V_3\frac{\partial\Theta_1}{\partial y}\right]\\ &\quad + Pr\,V_2\left[Ra_{p,L}\frac{\partial\theta_{L2}}{\partial y}\cos X + Ra_{p,U}\frac{\partial\theta_{U2}}{\partial y}\cos(X+\Omega)\right]\\ &\quad + Pr\,V_4\left[Ra_{p,L}\frac{\partial\theta_{L0}}{\partial y}\cos X + Ra_{p,U}\frac{\partial\theta_{U0}}{\partial y}\cos(X+\Omega)\right] - \frac{\partial^2\Theta_2}{\partial X^2}. \quad (4.15)\end{aligned}$$

Extraction of the aperiodic part of the forcing on the right-hand side of (4.15) and determination of the aperiodic part of the solution lead to the final approximation of the average Nusselt number of the form

$$\begin{aligned}Nu_{av} &= \alpha^2\left[\frac{1}{1400}(Ra_{p,L}^2 + Ra_{p,U}^2) + \frac{17}{12\,600}Ra_{p,L}Ra_{p,U}\cos\Omega\right]\\ &\quad - \alpha^4\left\{\frac{1}{283\,500}[208(Ra_{p,L}^2 + Ra_{p,U}^2) + 409\,Ra_{p,L}Ra_{p,U}\cos\Omega]\right.\\ &\quad + \frac{Re^2}{12\,770\,257\,500}[(12\,315 + 3130\,Pr + 1104\,762\,Pr^2)(Ra_{p,L}^2 + Ra_{p,U}^2)\\ &\quad \left. + 2(11\,835 + 3095\,Pr + 1102\,113\,Pr^2)\,Ra_{p,L}Ra_{p,U}\cos\Omega]\right\}\\ &\quad + O(\alpha^6). \quad (4.16)\end{aligned}$$

The heat always flows from the lower wall to the upper wall regardless where the heating is applied. Heating of one of the walls, regardless which wall is heated, results in the same heat flux. The heat flux consists of separate contributions associated with the upper and lower wall heating (terms proportional to $Ra_{p,L}^2$ and $Ra_{p,U}^2$), and of interactions between these heatings (terms proportional to the product $Ra_{p,L}Ra_{p,U}$). The interaction terms increase the heat flow for $0 < \Omega < \pi/2$ and $3\pi/2 < \Omega < 2\pi$ and decrease it for $\pi/2 < \Omega < 3\pi/2$. The maximum heat flux is achieved with $\Omega = 0$ and it is much larger than can be achieved with one-wall heating. The minimum corresponds

to $\Omega = \pi$ and is smaller than can be achieved with one-wall heating. The net heat flow decreases as $\alpha^2$ when $\alpha \to 0$ regardless of $\Omega$.

The structure of the above solution suggests different mechanics governing the heat transfer and the drag reduction. The external heating creates periodic modulations of the flow and temperature field (see (4.5)). Interactions between the conductive and convective modulations create the net heat flow across the channel at $O(\alpha^2)$ and further periodic modulations of the velocity and temperature fields (see (4.7)). Additional periodic modulations are added at the $O(\alpha^3)$ approximation. Finally, the nonlinear interactions between the velocity field modulations create the pressure gradient correction which occurs at $O(\alpha^4)$ (see (4.10)). This suggests that the largest heat flow will occur for $\alpha$ producing the most effective interactions between the conductive temperature modulations and the primary flow field modulations. The largest drag reduction will occur for $\alpha$ leading to the most effective nonlinear interactions between the flow field modulations. These two $\alpha$ are not the same as will be demonstrated in the next section.

## 5. Heating with an arbitrary wavenumber

It has been shown (Hossain *et al.* 2012; Floryan & Floryan 2015) that periodic heating applied at the lower wall reduces the pressure loss proportionally to $\alpha^{-7}$ when $\alpha \to \infty$. Because of the length of the relevant solution, we shall rely on the numerical demonstration to show that the same law applies to two-wall heating.

### 5.1. *Drag reduction*

We begin the discussion with the demonstration that the same periodic heating applied either at the lower or at the upper wall results in identical drag reduction regardless of the heating wavenumber.

The drag reduction is associated with the formation of separation bubbles which (i) insulate the stream from direct contact with the bounding walls and (ii) provide propulsion due to the fluid rotation inside of the bubbles which is driven by the horizontal density gradients. Figure 2(*a*) illustrates a typical flow pattern when the heating is applied at the lower wall while figure 2(*b*) illustrates the symmetric pattern when the same heating is applied to the upper wall. Both patterns are topologically identical and produce the same drag reduction. They display the up–down symmetry when combined with the horizontal phase shift of $\lambda/2$.

The flow topologies resulting from the simultaneous application of the same heating at both walls are illustrated in figure 3. It can be seen that the size of the separation bubbles, as well as the intensity of the motion inside of the bubble, depend on the phase shift between both heating patterns; they are largest for $\Omega = 0$ (figure 3*a*) and larger than those found in the case of the single-wall heating, and smallest for $\Omega = \pi$ (figure 3*e*) and smaller than in the case of the single-wall heating. This result demonstrates the potential for increase of the drag reduction through judicious selection of $\Omega$. The flow topologies display the up–down symmetries combined with the horizontal phase shifts. $\Omega = \pi$ (figure 3*e*) produces a simple symmetry without any phase shifts, $\Omega = 3\pi/4$ (figure 3*d*) has up–down symmetry with $\Omega = 5\pi/4$ (figure 3*f*) when combined to the phase shift of $\lambda/8$, $\Omega = \pi/2$ (figure 3*c*) has the up–down symmetry with $\Omega = 3\pi/2$ (figure 3*g*) when combined with the phase shift of $\lambda/4$ and $\Omega = \pi/4$ (figure 3*b*) has the up–down symmetry with $\Omega = 7\pi/4$ (figure 3*h*) when combined with the phase shift of $\lambda/8$. Topologies with the up–down

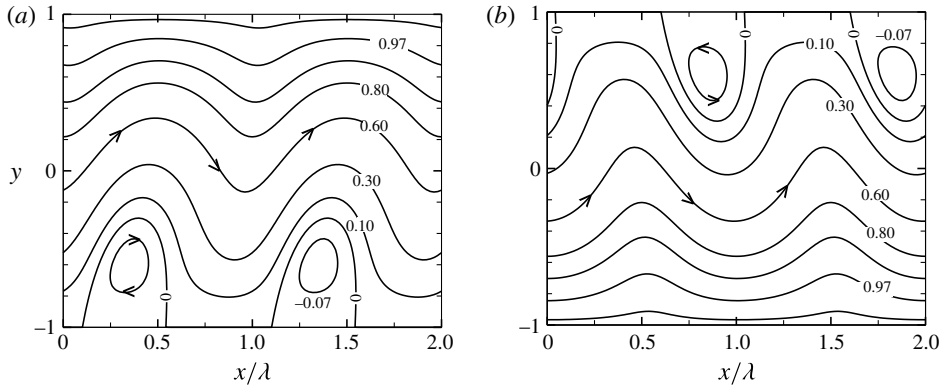


FIGURE 2. The flow topologies resulting from the heating applied either at the lower wall (*a*) with $Ra_{p,L} = 1000$, $Ra_{p,U} = 0$ or at the upper wall (*b*) with $Ra_{p,L} = 0$, $Ra_{p,U} = 1000$ for $Re = 5$, $\alpha = 2.5$, $Pr = 0.71$. Values of the stream function are normalized with its maxima; $\psi_{max} = 6.67$ for each case. The pressure gradient corrections are $A = 0.8316$ in each case.

symmetries and the proper phase shifts have the same global characteristics, e.g. the same drag reduction.

Figure 4 illustrates variations of the wall shear stress for different relative positions of the upper and lower heatings. In all cases, the magnitude of the shear stress is much higher than that found in the isothermal channel. The shear stress distributions have symmetries similar to the flow symmetries discussed above. While magnitudes of the lower wall shear stress in the two-wall heating case are not too dissimilar from those obtained by applying heating to the lower wall only, there is an order of magnitude increase in the shear stress acting at the upper wall. Figure 5(*a*) displays variations of the modifications of the mean shear stress as functions of the phase shift $\Omega$. Shear stress at the lower wall contributes to drag reduction for $\Omega \in [0, 0.27]$ and $\Omega \in [3.11, 2\pi]$, and to drag increase for $\Omega \in [0.27, 3.11]$. Shear stress at the upper wall contributes to drag reduction for $\Omega \in [0, 3.17]$ and $\Omega \in [6.02, 2\pi]$, and to drag increase for $\Omega \in [3.17, 6.02]$. Both mean shear stresses exhibit large variations as a function of $\Omega$, including changes in direction, but their sum, which captures the total effect, is much smaller than the individual shear stresses. This sum demonstrates that the heating always reduces drag. Figure 5(*b*) illustrates variations of the pressure gradient correction $A$ which is equal to half of the sum of the mean shear stresses displayed in figure 5(*a*) (see (3.16)). The largest $A$ corresponds to $\Omega = 0$ and is approximately 2.5 times larger than reduction achieved with only one-wall heating. The smallest $A$ corresponds to $\Omega = \pi$ and is approximately half of that achieved with the one-wall heating. The largest drag reduction is achieved in a small range of $\Omega$ centred around $\Omega = 0$ as $A$ is fairly insensitive to small changes of $\Omega$ in this zone. Larger phase shifts between the heating patterns away from their most effective position ($\Omega = 0$) result in a rapid reduction of $A$. The symmetries of $A$ in the $\Omega$ direction are similar to those of the mean wall shear stresses discussed above.

Figure 6 illustrates the distribution of the shear stress along the walls for different $\alpha$ values for the most effective $\Omega$, i.e. $\Omega = 0$. The shear stress changes from negative to positive over one heating wavelength and its amplitude is significantly larger than the magnitude of the isothermal shear stress. This amplitude reaches a maximum for $\alpha \approx 1$ and its distribution attains a nearly trapezoidal form with the shear stress rapidly

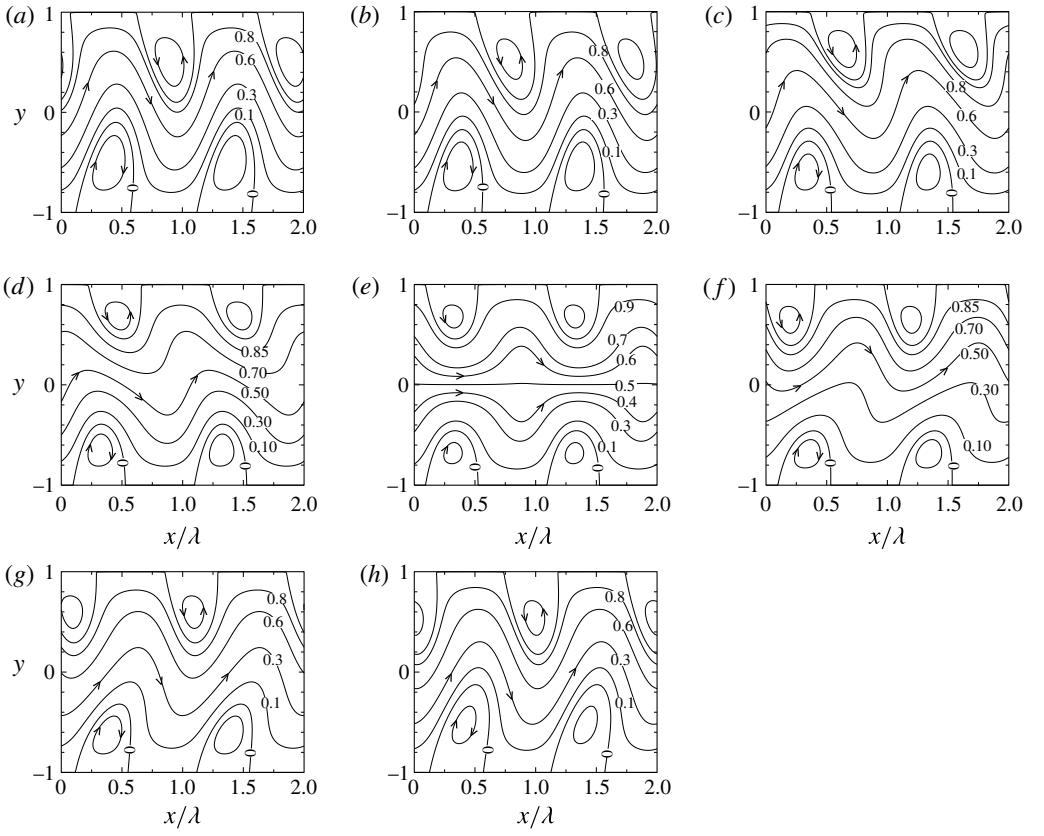


FIGURE 3. Flow topologies resulting from the same heating patterns applied at both walls with $Ra_{p,L} = Ra_{p,U} = 1000$, $Re = 5$, $\alpha = 2.5$, $Pr = 0.71$. (*a–h*) Display results for the phase shifts $\Omega = 0,\ \pi/4,\ \pi/2,\ 3\pi/4,\ \pi,\ 5\pi/4,\ 3\pi/2,\ 7\pi/4$, respectively. The corresponding maxima of the stream function $\psi_{max}$ are 7.69, 7.49, 7.21, 7.10, 7.14, 7.27, 7.45, 7.64, respectively, and the corresponding pressure gradient corrections $A$ are 2.6297, 2.3401, 1.6090, 0.8476, 0.5289, 0.8476, 1.6090, 2.3401, respectively. (*a*) $\Omega = 0$, $\psi_{max} = 7.69$, $A = 2.6297$; (*b*) $\Omega = \pi/4$, $\psi_{max} = 7.49$, $A = 2.3401$; (*c*) $\Omega = \pi/2$, $\psi_{max} = 7.21$, $A = 1.6090$; (*d*) $\Omega = 3\pi/4$, $\psi_{max} = 7.10$, $A = 0.8476$; (*e*) $\Omega = \pi$, $\psi_{max} = 7.14$, $A = 0.5289$; (*f*) $\Omega = 5\pi/4$, $\psi_{max} = 7.27$, $A = 0.8476$; (*g*) $\Omega = 3\pi/2$, $\psi_{max} = 7.45$, $A = 1.6090$; (*h*) $\Omega = 7\pi/4$, $\psi_{max} = 7.64$, $A = 2.3401$.

changing directions around $x = 0$ and $x = \lambda/2$. Reduction of $\alpha$ causes a rapid decrease of the amplitude with the distribution evolving towards a sinusoidal form. Increase of $\alpha$ also causes a reduction of the amplitude, but at a much slower rate, and evolution of the distribution towards a sinusoidal form. The reader may note that such evolution of shear stress is related to the shape of the bubbles. In the case of long and short bubbles, the finite height of the channel does not affect their shape directly; in the former case the bubbles attain asymptotic form described by the solution given in § 4 while in the latter cases they begin to be dominated by phenomena taking place in the boundary layers developing near the walls (see Floryan & Floryan 2015) with the channel height being less important. When $\alpha \approx 1$, the shape of the bubbles is directly affected by the channel height.

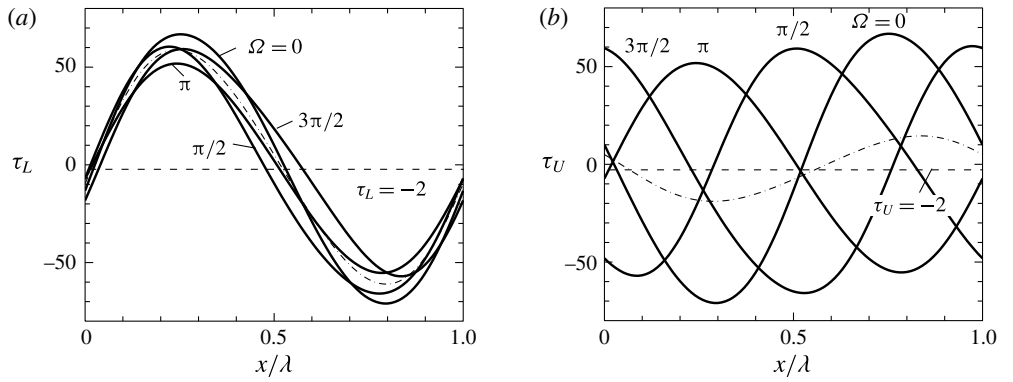


FIGURE 4. Shear stress distributions at the lower (*a*) and upper (*b*) walls for the two-wall heating with $Ra_{p,L} = Ra_{p,U} = 1000$ for $\alpha = 2.5$, $Re = 1$, $Pr = 0.71$. The dashed-dotted line gives the shear stress distributions for the lower-wall heating only. The dashed lines illustrate the shear stress for the isothermal channel ($\tau_U = \tau_L = -2Re = -2$). The average stresses for the two-wall heating for $\Omega = 0$, $\pi/2$, $\pi$, $3\pi/2$ are $\tau_{L,ave} = -1.12$, $-5.5$, $-1.86$, $2.88$, $\tau_{U,ave} = -1.12$, $2.88$, $-1.86$, $-5.5$, respectively. The average stresses for the lower-wall heating are $\tau_{L,ave} = -1.05$, $\tau_{U,ave} = -2.25$.

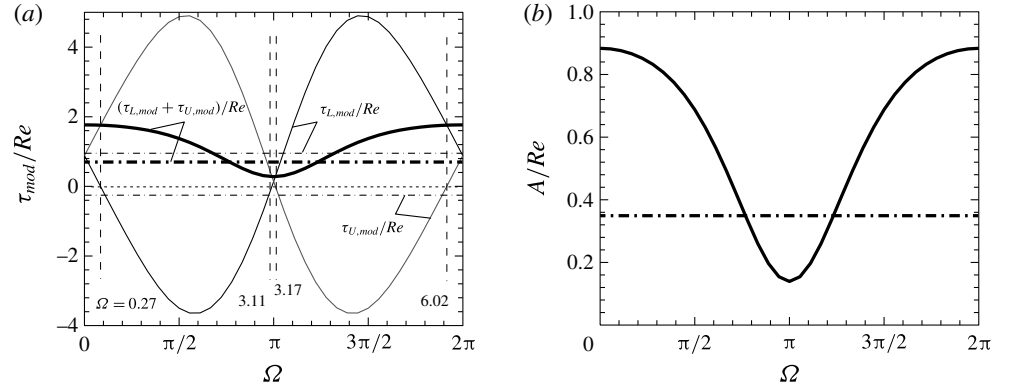


FIGURE 5. Variations of the heating-induced modification of the average shear stresses at the lower ($\tau_{L,mod}/Re$) and upper ($\tau_{U,mod}/Re$) walls (see (3.15)) as well as their sum (*a*) and the pressure gradient correction $A/Re$ (*b*) as a function of the phase shift $\Omega$ for $Ra_{p,L} = Ra_{p,U} = 1000$, $\alpha = 2.5$, $Re = 1$, $Pr = 0.71$. The solid lines correspond to the two-wall heating and the dashed-dotted lines correspond to the lower-wall heating. The thick lines correspond to the combined effect of heating of both walls. The dotted line in (*a*) identifies the reference point $\tau_{mod} = 0$. The reader may note that $(\tau_{L,mod} + \tau_{U,mod})/Re$ from (*a*) is equal to $2A/Re$ from (*b*).

The magnitude of the shear stress acting at the lower wall is similar to that found for the lower-wall heating only, while the magnitude of the shear stress acting at the upper wall is significantly larger than in the lower-wall heating case. Figure 7 illustrates cumulative effects, i.e. variations of the modifications of the mean shear stress $\tau_{mod}$ (see (3.15)) as a function of $\alpha$. It can be seen that the modifications peak around $\alpha \approx 2.5$ and decrease rapidly for both large and small $\alpha$. The decrease for small $\alpha$ has been explained in § 4. The decrease for large $\alpha$ is associated with the

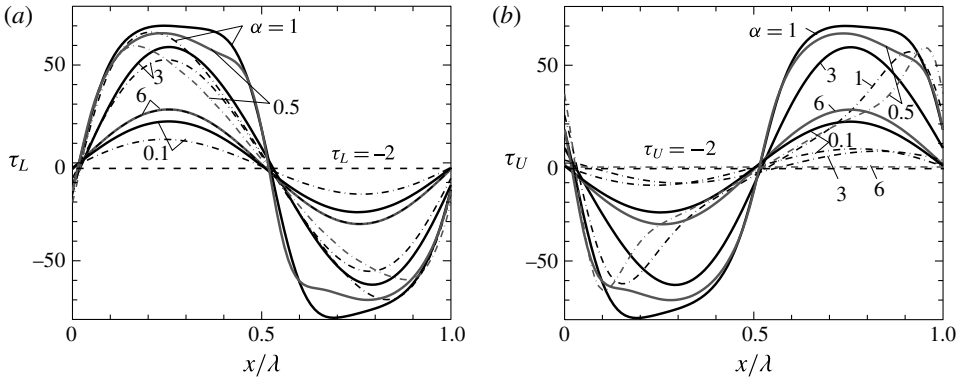


FIGURE 6. Shear stress distributions at the lower (*a*) and upper (*b*) walls for different heating wavenumbers $\alpha$ for $\Omega = 0$, $Re = 1$, $Pr = 0.71$, $Ra_{p,L} = Ra_{p,U} = 1000$. The solid, dashed-dotted and dashed lines correspond to the two-wall heating, the lower-wall heating and the isothermal channel, respectively. The average stresses for the two-wall heating for $\alpha = 0.1$, 0.5, 1, 3, 6 are $\tau_{L,ave} = \tau_{U,ave} = -1.99, -1.93, -1.83, -1.12, -1.98$, respectively; the average stresses for the lower-wall heating for $\alpha = 0.1$, 0.5, 1, 3, 6 are $\tau_{L,ave} = -1.99, -1.81, -1.40, -1.39, -1.98$ and $\tau_{U,ave} = -2.00, -2.13, -2.36, -2.09, -1.99$, respectively. Lines for $\tau_{L,ave}$ for $\alpha = 6$ for the lower-wall heating and two-wall heating overlap in (*a*).

formation of boundary layers adjacent to the heated walls (Hossain & Floryan 2015*a*). The character of the variations of $\tau_{mod}$ for $\alpha = O(1)$ is however very complex and depends on $\Omega$. Both mean shear stresses contribute to the drag reduction for $\Omega = 0$, their variations as a function of $\alpha$ are fairly smooth and the maxima are similar on both walls (see figure 7*a*). When $\Omega = \pi/4$ variations of both shear stresses are vastly different, the lower-wall shear stress contributes to the drag increase, the upper-wall shear stress contributes to the drag decrease and the overall effect is drag reduction as the upper-wall shear stress brings in a larger contribution (see figure 7*a*). At $\Omega = \pi$ the process is similar to $\Omega = 0$, i.e. both mean shear stresses contribute to the drag reduction, but they are so small that the net effect is less than what can be achieved with the one-wall heating (see figure 7*b*). The cumulative effects exhibit smooth variations as a function of $\alpha$ for all $\Omega$ in spite of huge differences in the shear stresses acting at both walls (see figure 7).

Figure 8 illustrates variations of the pressure gradient correction as a function of $\alpha$. The drag reduction is clearly visible but its magnitude rapidly decreases for $\alpha$ values which are either too large or too small, i.e. this decrease is proportional to $\alpha^4$ when $\alpha \to 0$ (see § 4) and to $\alpha^{-7}$ when $\alpha \to \infty$ (Floryan & Floryan 2015; Hossain & Floryan 2015*a*). A significant increase of the drag reduction, as compared to what can be achieved using the single-wall heating, is clearly demonstrated but only if one uses a proper phase difference between both heating patterns. This increase may reach up to 300 %. Use of the improper phase difference significantly weakens this effect and can lead to drag reduction smaller than that which can be achieved using the one-wall heating.

We begin the discussion of the effects of the Reynolds and Rayleigh numbers by looking at the evolution of the flow patterns as functions of these two parameters (figures 9 and 10). Increase of $Re$ for a fixed $Ra_p$ reduces the size of the separation bubbles as well as the intensity of the motion in their interior; the bubbles are

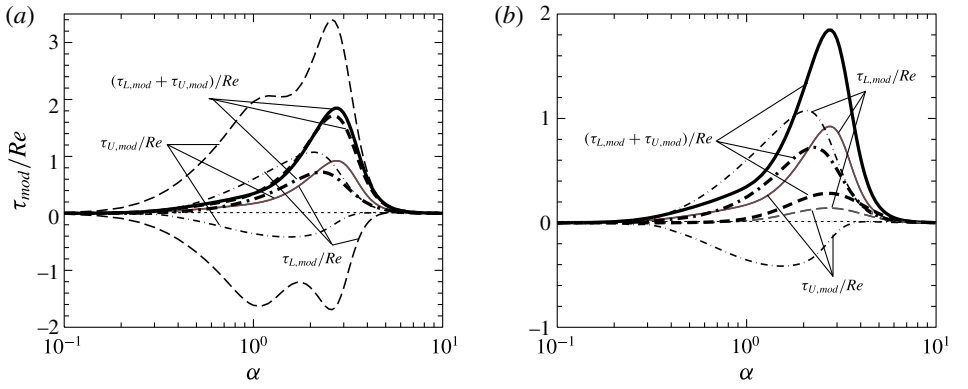


FIGURE 7. Variations of the heating-induced modifications of the average shear stresses at the lower ($\tau_{L,mod}/Re$) and upper ($\tau_{U,mod}/Re$) walls (see (3.15)) as well as their sum $(\tau_{L,mod}+\tau_{U,mod})/Re$ as functions of the heating wavenumber $\alpha$ for $Ra_{p,L}=Ra_{p,U}=1000$, $Re=1$, $Pr=0.71$. (*a*) Displays data for $\Omega=0$ (solid lines) and $\Omega=\pi/4$ (dashed lines) while (*b*) displays data for $\Omega=0$ (solid lines) and $\Omega=\pi$ (dashed lines). The dashed-dotted lines in both figures correspond to the lower-wall heating. The thick lines identify the cumulative effect $(\tau_{L,mod}+\tau_{U,mod})/Re$. The dotted lines give the reference point $\tau_{mod}=0$. Lines for $\tau_{U,mod}/Re$ and $\tau_{L,mod}/Re$ overlap when $\Omega=0,\ \pi$.

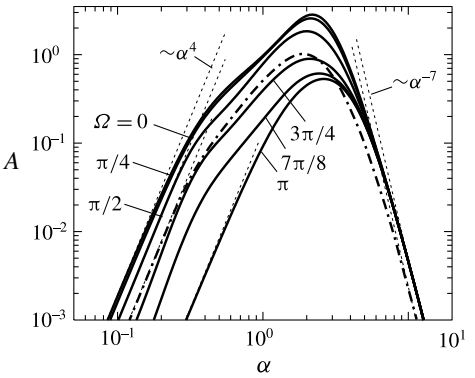


FIGURE 8. Variation of the pressure gradient correction $A$ as a function of the heating wavenumber $\alpha$ for $Ra_{p,L}=Ra_{p,U}=1000$, $Re=5$, $Pr=0.71$ and selected phase angles $\Omega$. The dashed-dotted lines correspond to the single-wall heating. Asymptotes are marked using dotted lines.

washed away for $Re>20$ when $Ra_{p,L}=Ra_{p,U}=1000$ as illustrated in figure 9. The bubbles can survive a stronger flow if one increases the heating intensity. Figure 10 provides information about the minimum Rayleigh number required in order to create various flow topologies. This particular figure displays data for both walls exposed to the same heating intensity with the phase shift $\Omega=0$. The reader may note that bubbles at the upper wall persist to much higher $\alpha$ when both walls are exposed to the heating compared with the single-wall heating. The structure of the bubbles at the lower wall is similar for both types of heating. The same data plotted using the Richardson numbers $Ri_{p,L}=Ra_{p,L}/(Pr^*Re^2)$ and $Ri_{p,U}=Ra_{p,U}/(Pr^*Re^2)$ rather than Rayleigh numbers do not provide better insights and thus are not shown.

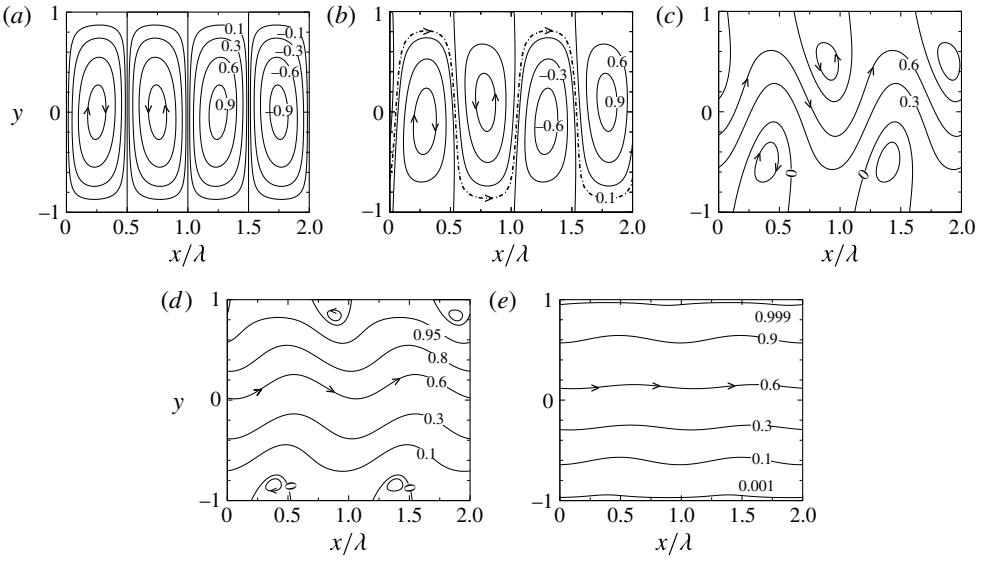


FIGURE 9. Flow topologies resulting from identical heatings applied at both walls with $Ra_{p,L} = Ra_{p,U} = 1000$, $\Omega = 0$, $\alpha = 2.5$, $Pr = 0.71$. (*a–e*) Display results for $Re = 0$, 1, 5, 10, 20, respectively. The corresponding maxima of the stream function are $\psi_{max} = 4.28$, 4.94, 7.69, 13.4, 26.67, respectively, and the corresponding pressure gradient corrections are $A = 0$, 0.8835, 2.6297, 1.4271, 0.4119, respectively. The corresponding quantities for the single-wall heating are $(\psi_{max}, A) = (2.5793, 0)$, (2.9386, 0.3491), (6.6667, 0.8316), (13.3333, 0.4971), (26.6667, 0.1716). (*a*) $Re = 0$, $\psi_{max} = 4.28$, $A = 0$; (*b*) $Re = 1$, $\psi_{max} = 4.94$, $A = 0.8835$; (*c*) $Re = 5$, $\psi_{max} = 7.69$, $A = 2.6297$; (*d*) $Re = 10$, $\psi_{max} = 13.4$, $A = 1.4271$; (*e*) $Re = 20$, $\psi_{max} = 26.67$, $A = 0.4119$.

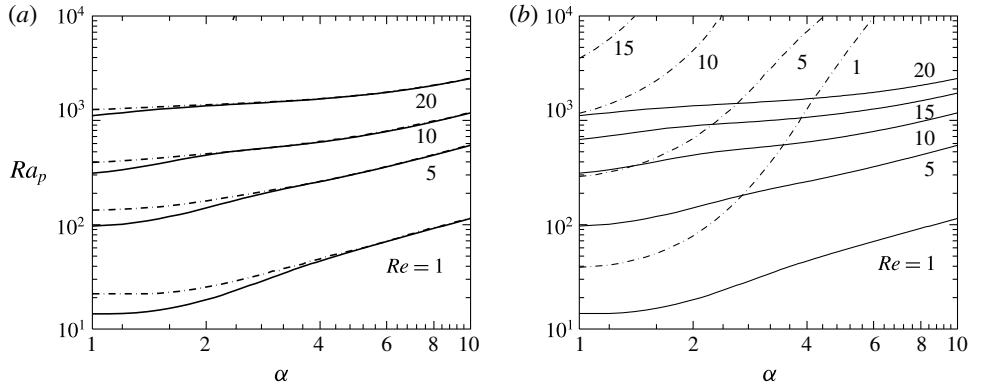


FIGURE 10. The minimum Rayleigh number $Ra_p = Ra_{p,L} = Ra_{p,U}$ required for the formation of the separation bubbles at the lower (*a*) and upper (*b*) walls for $\Omega = 0$, $Pr = 0.71$. The solid lines correspond to the two-wall heating while the dashed-dotted lines correspond to the lower-wall heating.

Figure 11 displays distributions of the wall shear stress over one heating wavelength for different *Re*'s starting with $Re = 0$. The amplitude of the shear stress variations along the walls decreases as *Re* increases and its reduction correlates well with the

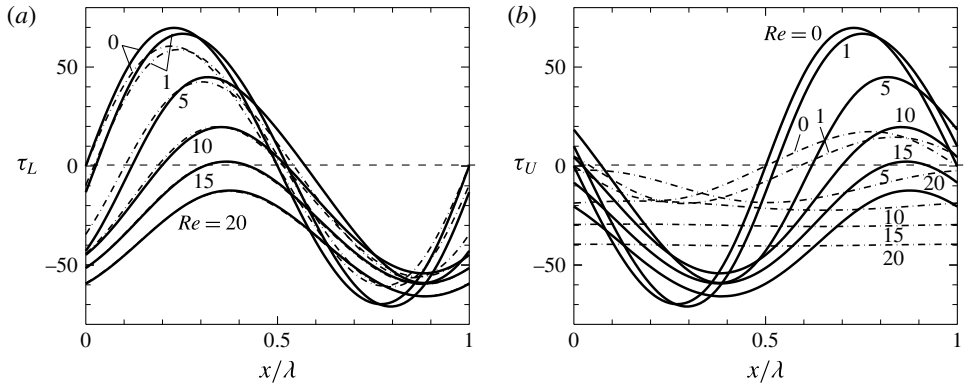


FIGURE 11. Shear stress distributions at the lower (*a*) and upper (*b*) walls for different Reynolds numbers $Re$ for $\Omega = 0$, $\alpha = 2.5$, $Pr = 0.71$, $Ra_{p,L} = Ra_{p,U} = 1000$. The solid and dashed-dotted lines correspond to the two-wall heating and the lower-wall heating, respectively. The average stresses for $Re = 0$, 1, 5, 10, 15, 20 in the former case are $\tau_{L,ave} = \tau_{U,ave} = 0$, $-1.12$, $-7.37$, $-18.57$, $-29.28$, $-39.59$ and in the latter case are $\tau_{L,ave} = 0$, $-1.0487$, $-8.0239$, $-19.01$, $-29.4973$, $-39.71$ and $\tau_{U,ave} = 0$, $-2.25$, $-10.31$, $-20.0$, $-29.94$, $-39.95$. The average shear stress for the isothermal channel is $-2Re$. The dashed lines provide the reference points $\tau_L = 0$ and $\tau_U = 0$.

washing away of the separation bubbles illustrated in figure 9. The amplitudes of the shear stress at the lower wall are nearly similar for the one-wall and the two-wall heatings but the amplitudes at the upper wall are vastly different. Figure 12 illustrates changes in the heating-induced shear stress modification at the lower and upper walls as well as the cumulative effect. The modifications have the same magnitude but opposite directions in the limit of $Re \to 0$ and result in the thermally induced drift (Hossain & Floryan 2015*b*). They evolve differently at the upper and lower walls as $Re$ increases, providing the net force which assists the fluid movement. The maximum effect occurs for $Re \approx 6$ for the particular conditions used in this figure. Further increase of $Re$ reduces the drag reducing effect and the shear stress modifications practically vanish at $Re \approx 50$. The resulting pressure gradient corrections are illustrated in figure 13. The correction increases linearly for small $Re$, as predicted in § 4, the growth saturates at $Re \approx 6$ and is followed by a rapid decrease. Since the magnitude of the pressure gradient for the isothermal flow increases proportionally to $Re$ (3.16), the pressure gradient correction represents a constant fraction of the isothermal pressure gradient for small enough $Re$. Variations of $A$ are similar for the whole range of Rayleigh numbers considered in this analysis with the higher magnitudes achieved for higher $Ra_p$'s. Data displayed in figure 14 demonstrate that the most effective heating wavenumber, as far as the drag reduction is concerned, is $\alpha \approx 2.7$ for the most effective phase shifts ($\Omega = 0$). The drag reduction is up to three times larger than the reduction which can be achieved with one-wall heating.

The effectiveness of the heating intensity can be judged using data displayed in figure 15. The pressure gradient correction initially increases proportionally to $Ra_p^2$, which conforms to the analytical prediction given by (4.14). The growth eventually saturates and a further increase of $Ra_p$ results in a reduction rather than any further increase of the pressure gradient correction. The reader may note that it is possible to create a pressure gradient correction which is larger than the isothermal pressure gradient, i.e. it is possible to use wall heating to pump the fluid without the use of

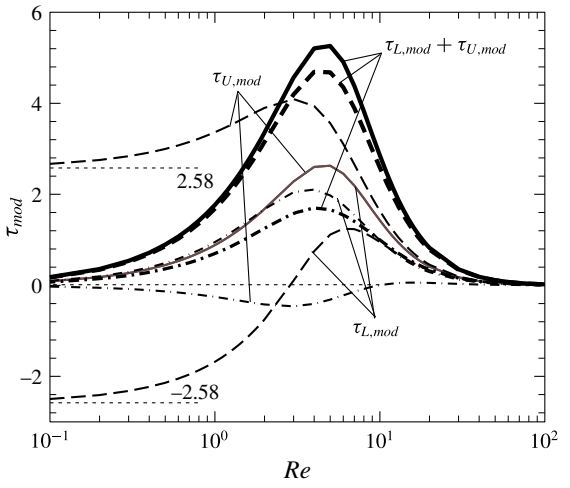


FIGURE 12. Variations of the heating-induced modifications of the average shear stresses at the lower wall $\tau_{L,mod}$ (see (3.15)), the upper wall $\tau_{U,mod}$ (see (3.15)) as well as their sum $\tau_{L,mod} + \tau_{U,mod}$ as functions of the Reynolds number $Re$ for $\Omega = 0$ (solid lines) and $\pi/4$ (dashed lines), $Ra_{p,L} = Ra_{p,U} = 1000$, $\alpha = 2.5$, $Pr = 0.71$. Dashed-dotted lines correspond to the lower-wall heating. Thick lines identify the cumulative effect, i.e. $\tau_{L,mod} + \tau_{U,mod}$. The dotted line provides the reference point $\tau_{mod} = 0$.

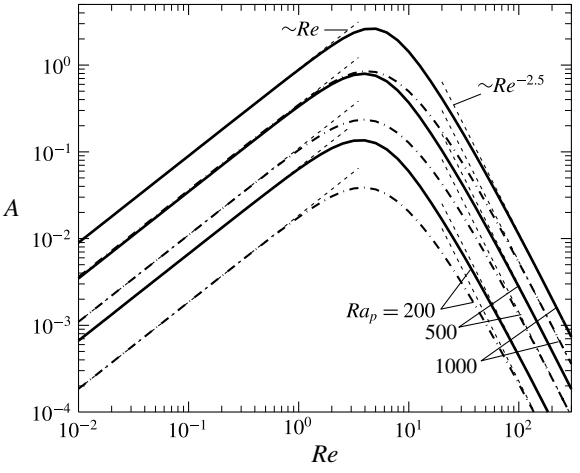


FIGURE 13. Variation of the pressure gradient correction $A$ as a function of the Reynolds number $Re$ for selected heating intensities $Ra_p = Ra_{p,L} = Ra_{p,U}$ for $\alpha = 2.5$, $Pr = 0.71$ and $\Omega = 0$. The solid and dashed-dotted lines correspond to the two-wall heating and the single-wall heating, respectively. Asymptotes are marked using dotted lines.

any externally applied pressure gradient. The magnitude of the required $Ra_p$ is such that the temperature differences that the fluid is exposed to would prevent the use of the Boussinesq model and the variations of the fluid thermal properties would have to be accounted for. The most effective heating wavenumber as far as the drag reduction is concerned shifts from $\alpha \approx 1.6$ for $Ra_p \approx 100$ to $\alpha \approx 2.7$ for $Ra_p \approx 1000$ as illustrated in figure 16 for $\Omega = 0$.

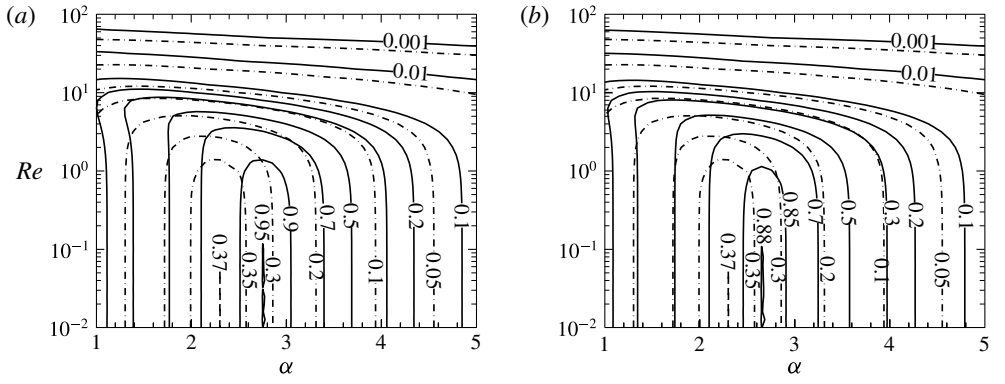


FIGURE 14. Variation of the pressure gradient correction $A/Re$ as a function of the heating wavenumber $\alpha$ and the flow Reynolds number $Re$ for $Ra_{p,L} = Ra_{p,U} = 1000$, $Pr = 0.71$, and phase angles $\Omega = 0$ ($a$) and $\Omega = \pi/4$ ($b$). The dashed-dotted lines correspond to the single-wall heating.

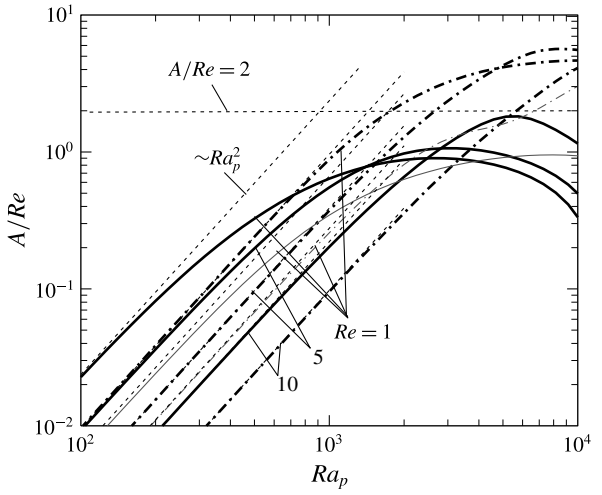


FIGURE 15. Variation of the pressure gradient correction $A/Re$ as a function of the Rayleigh number $Ra_p = Ra_{p,L} = Ra_{p,U}$ for $\Omega = 0$, $Pr = 0.71$ and $\alpha = 2$ (thick solid lines) and $\alpha = 3$ (thick dashed-dotted lines). Dotted lines identify the small-$Ra_p$ asymptotes. Thin solid and dashed-dotted lines correspond to the single-wall heating.

The above discussion demonstrates that the spatially periodic heating represents an effective mechanism for reduction of the pressure gradient required to maintain the desired flow rate. One can consider two types of applications of this phenomenon. In the first type, one is interested in the drag reduction in order to save the energy required to pump the fluid. The required heating comes with an energy cost but the question of the net gain, i.e. determination of whether the reduction of the required pressure gradient overcomes the costs of creation of the required heating/cooling, is difficult to answer. It is known that the overall viscous dissipation in an isothermal channel under a constant flow rate reaches a minimum for the laminar parabolic profile (Bewley 2009; Fukagata, Sugiyama & Kasagi 2009) and thus the overall

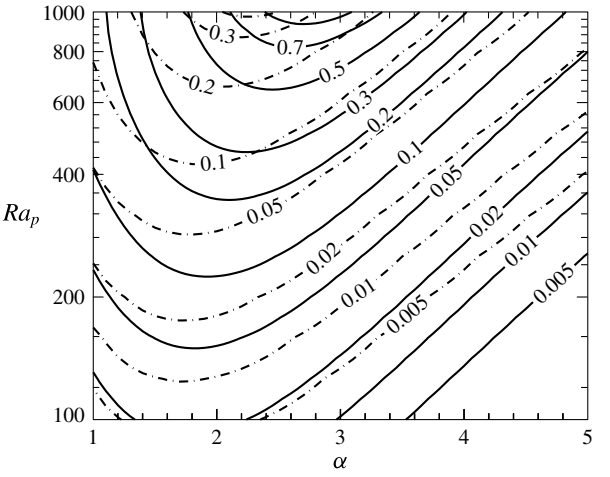


FIGURE 16. Variation of the pressure gradient correction $A/Re$ as a function of the heating wavenumber $\alpha$ and the periodic Rayleigh numbers $Ra_{p,L} = Ra_{p,U} = Ra_p$ for $Re = 1$, $Pr = 0.71$, $\Omega = 0$. The dashed-dotted lines correspond to the single-wall heating.

energy consumption is always higher for the controlled flow than that of the uncontrolled flow. This statement likely applies to the non-isothermal channels in spite of the lack of any formal proof. The cost of creation of the heating pattern is a strong function of the heating technique but could be marginal if the heat supply is sufficiently inexpensive, e.g. waste heat. In the second type of applications, the required pressure difference between the channel entrance and the channel exit is too high to be efficiently created using standard techniques and its magnitude could be large enough to cause structural deformations of the conduit. In such cases, one is looking for alternative pumping methods where the propulsive force is distributed along the channel length. The interdependence between the pumping power and the drag reduction is well explained by Hœpffner & Fukagata (2009). The peristaltic pumping provides a good example of a technique with a distributed propulsive force (Takagi & Balmforth 2011). The heating-induced drag reduction can be viewed as an alternative. In this case, the energy cost associated with the creation of the temperature patterns comes as a secondary consideration but nevertheless one is interested in the relevant heat transfer characteristics. We shall now discuss these characteristics.

### 5.2. *Heat transfer*

The average Nusselt number $Nu_{av}$ describes the net heat transfer between the walls and can be viewed as the direct energy cost of the heating-induced drag reduction. It changes by 150 % as $\Omega$ varies from $\Omega = \pi$, which produces the lowest $Nu_{av} \approx 100$, to $\Omega = 0$, which produces the largest $Nu_{av} \approx 250$, as illustrated in figure 17. $Nu_{av}$ achieved with the two-wall heating is always larger than $Nu_{av}$ achieved with the one-wall heating (see figure 17). Data presented in figure 18 demonstrates that $\alpha \approx 1$ is the most effective for the maximization of $Nu_{av}$ for the majority of phase shifts $\Omega$ except in the vicinity of $\Omega \approx \pi$ where $\alpha \approx 2$ becomes the most effective. $Nu_{av}$ decreases proportionally to $\alpha^2$ when $\alpha \to 0$ (see § 4) and proportionally to $\alpha^{-3}$ when $\alpha \to \infty$ (Floryan & Floryan 2015; Hossain & Floryan 2015*a*). There is a lack of any relation between the most effective $\alpha$ values for the drag reduction and for the heat transfer

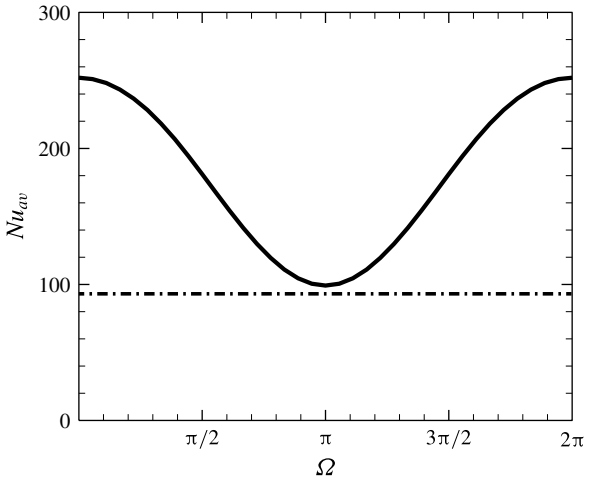


FIGURE 17. Variations of the average Nusselt number $Nu_{av}$ as a function of the phase shift $\Omega$ for $Ra_{p,L} = Ra_{p,U} = 1000$, $\alpha = 2.5$, $Re = 1$, $Pr = 0.71$. The solid and the dashed-dotted lines correspond to the two-wall heating and the single-wall heating, respectively.

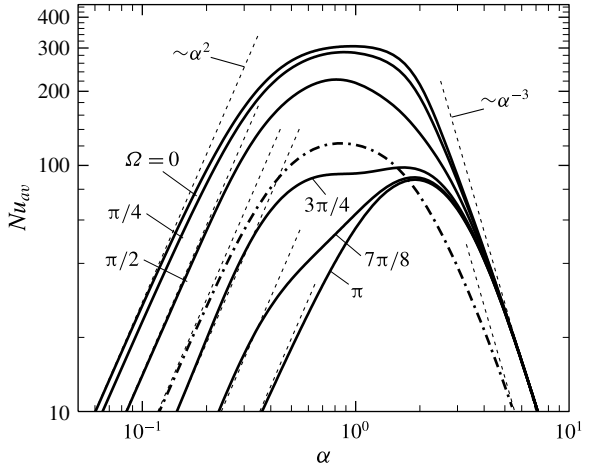


FIGURE 18. Variations of the average Nusselt number $Nu_{av}$ as a function of the heating wavenumber $\alpha$ for selected values of $\Omega$ for $Ra_{p,L} = Ra_{p,U} = 1000$, $Re = 5$, $Pr = 0.71$. The dashed-dotted line corresponds to the single-wall heating. Asymptotes are marked using dotted lines.

maximization, with $\alpha \approx 2$ being the most effective in the former case while $\alpha \approx 1$ being the most effective in the latter case (compare figures 8 and 18). This lack of correlation should not be surprising in view of the different processes leading to the generation of the heat flux and the pressure gradient correction discussed in § 4.

Variations of the Reynolds number do not affect the heat transfer as long as $Re < 6$. Further increase of $Re$ leads to a rapid decrease of $Nu_{av}$, as illustrated in figure 19. This behaviour is similar to variations of $A/Re$ discussed in the previous subsection. The decrease occurs in a similar manner for all $\alpha$ values (see figure 20) and is associated with the elimination of the separation bubbles which are responsible for

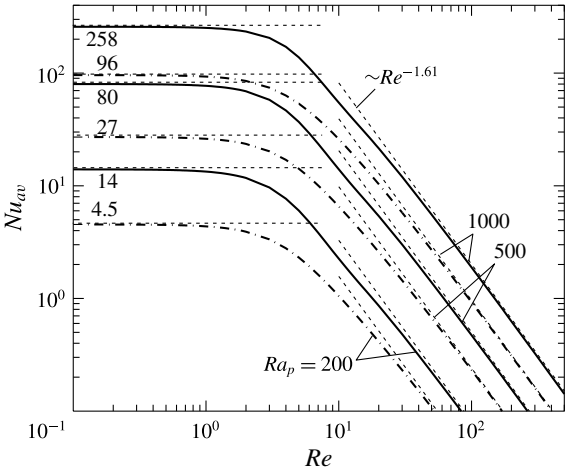


FIGURE 19. Variations of the average Nusselt number $Nu_{av}$ as a function of the Reynolds number $Re$ for $Ra_{p,L} = Ra_{p,U} = Ra_p = 200$, 500, 1000, and $\Omega = 0$, $\alpha = 2.5$, $Pr = 0.71$. Solid and dashed-dotted lines correspond to the two-wall heating and the single-wall heating, respectively. Asymptotes are marked using dotted lines.

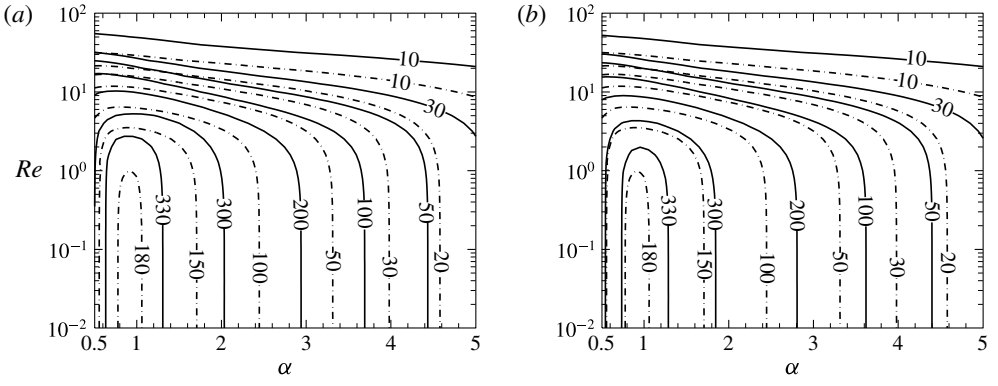


FIGURE 20. Variation of the average Nusselt number $Nu_{av}$ as a function of the heating wavenumber $\alpha$ and the flow Reynolds number $Re$ for $Ra_{p,L} = Ra_{p,U} = 1000$, $Pr = 0.71$, and phase angles $\Omega = 0$ (*a*) and $\Omega = \pi/4$ (*b*). Dashed-dotted lines correspond to the single-wall heating.

the transverse fluid movement. When the bubbles are washed away, the heat can be transferred between the walls by conduction only and, since the walls are subject to the periodic heating, the net heat transfer is eliminated. A rather small sensitivity of $Nu_{av}$ to variations of $\Omega$ is well illustrated by comparing results displayed in figure 20(*a*,*b*). Increase of $Ra_p$ results in an intensification of the convective motion and thus results in an increase of $Nu_{av}$ (see figure 21). The most effective $\alpha$ for the heat transfer maximization is independent of $Ra_p$ as demonstrated in figure 21.

The cost of moving energy within each wall in order to create the local hot and cold spots is difficult to assess but it obviously contributes to the overall energy cost. The quantity of energy which has to be moved can be determined by looking at the horizontal heat fluxes between the hot and cold wall segments and can be quantified

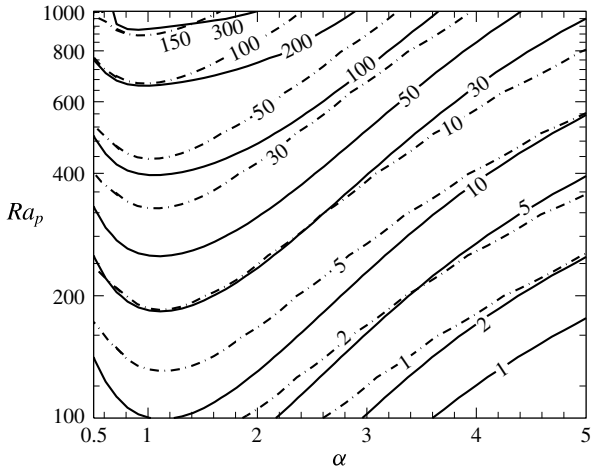


FIGURE 21. Variation of the average Nusselt number $Nu_{av}$ as a function of the heating wavenumber $\alpha$ and the periodic Rayleigh numbers $Ra_{p,L} = Ra_{p,U} = Ra_p$ for $Re = 1$, $Pr = 0.71$, $\Omega = 0$. Dashed-dotted lines correspond to the single-wall heating only.

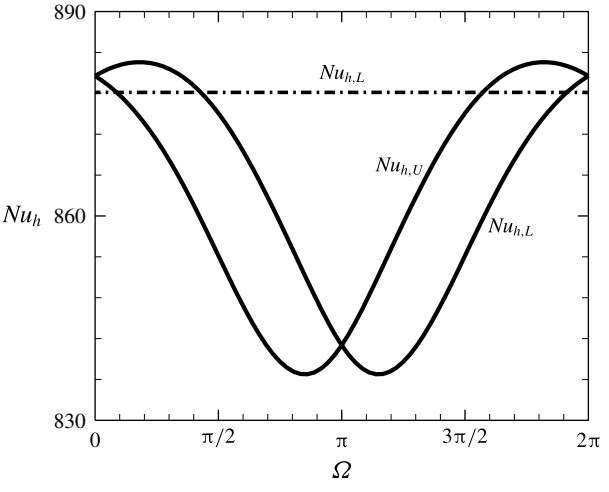


FIGURE 22. Variations of the upper ($Nu_{h,U}$) and lower ($Nu_{h,U}$) horizontal Nusselt numbers as functions of the phase shift $\Omega$ for $Ra_{p,L} = Ra_{p,U} = 1000$, $\alpha = 2.5$, $Re = 1$, $Pr = 0.71$. The solid lines and the dashed-dotted line correspond to the two-wall heating and the lower-wall heating only, respectively.

in terms of the heat flux leaving each wall per half heating wavelength and expressed by the horizontal Nusselt numbers defined in (3.19), i.e. in terms of $Nu_{h,L}$ and $Nu_{h,U}$. Results displayed in figure 22 demonstrate that both $Nu_{h,L}$ and $Nu_{h,U}$ change on the order of 5 % when $\Omega$ varies from 0 to $2\pi$ with $Nu_{h,L}$ achieving the highest magnitude for $\Omega = \pi/5$ and $Nu_{h,U}$ achieving the same value for $\Omega = 9\pi/5$. These magnitudes are slightly higher than in the case of the single-wall heating. Results displayed in figure 23 demonstrate that $Nu_{h,L}$ and $Nu_{h,U}$ remain independent of $Re$ for small $Re$'s where separation bubbles exist. Values of $Re$ which lead to the removal of the bubble result in an increase of $Nu_{h,L}$ and $Nu_{h,U}$ but this zone is of no interest for the drag

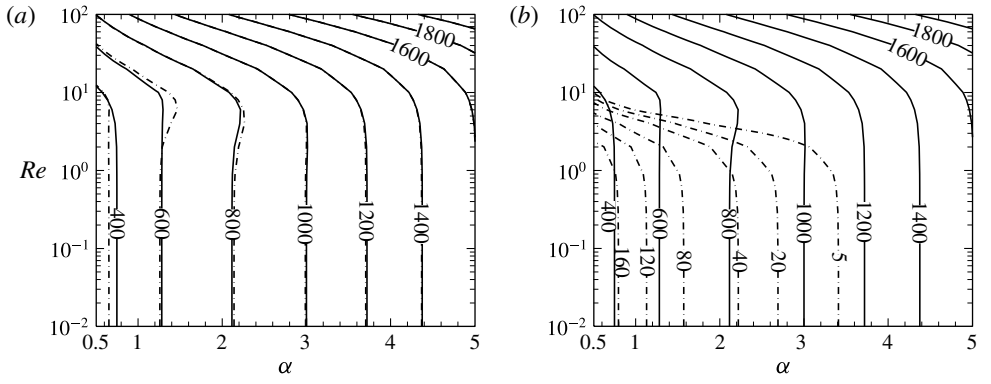


FIGURE 23. Variations of the horizontal Nusselt number $Nu_{h,L}$ at the lower wall ($a$) and the horizontal Nusselt number $Nu_{h,U}$ at the upper wall ($b$) as functions of the heating wavenumber $\alpha$ and the Reynolds number $Re$ for $Ra_{p,L} = Ra_{p,U} = Ra_p = 1000$, $Pr = 0.71$, $\Omega = 0$. Dashed-dotted lines correspond to the lower-wall heating only.

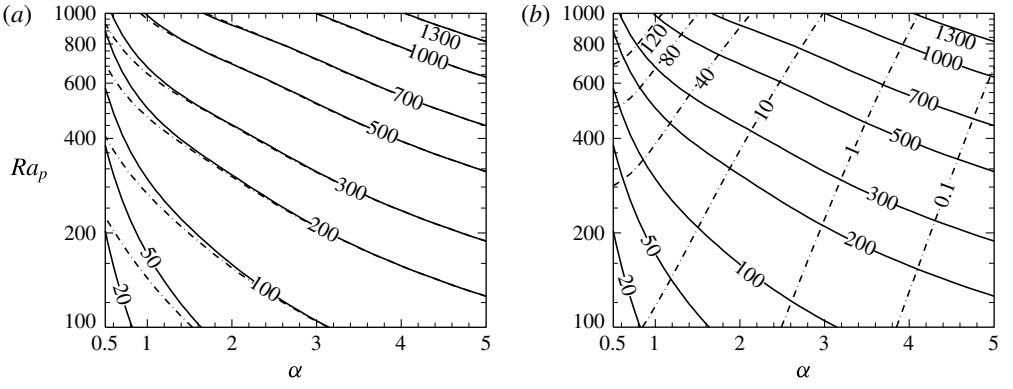


FIGURE 24. Variations of the horizontal Nusselt number $Nu_{h,L}$ at the lower wall ($a$) and the horizontal Nusselt number $Nu_{h,U}$ at the upper wall ($b$) as functions of the heating wavenumber $\alpha$ and the Rayleigh number $Ra_{p,L} = Ra_{p,U} = Ra_p$ for $Re = 1$, $Pr = 0.71$, $\Omega = 0$. Dashed-dotted lines correspond to the lower-wall heating only.

reducing applications. Increase of $\alpha$ also leads to an increase of $Nu_{h,L}$ and $Nu_{h,U}$ as temperature gradients imposed along the walls increase. The reader may note that the high values of $\alpha$ are also of no interest as they lead to the near elimination of the drag reducing effect. Values of $Nu_{h,L}$ are nearly the same whether single-wall or two-wall heatings are used while $Nu_{h,U}$ significantly increases when the single-wall heating is replaced by the two-wall heating. Increases of $Nu_{h,L}$ and $Nu_{h,U}$ as a function of $Ra_p$ are documented in figure 24 with $Nu_{h,L}$ being nearly the same for the single-wall and the two-wall heating while $Nu_{h,U}$ increases by an order of magnitude when the single-wall heating is replaced with the two-wall heating. These results suggest that the horizontal heat fluxes are driven by the thermal conditions prevailing at a given wall and are not affected by what happens at the other wall. A comparison of the conductive part of the heat flux, which can be determined analytically from (2.4), with the total heat flux demonstrates that the conductive effects provide the largest contributions to these fluxes.

The flow model used in the present analysis relies on the Boussinesq approximation and thus one needs to check the limits of its validity. The detailed calculations have been carried out for $Pr = 0.71$ (air) and most of the presented results were obtained for $Ra_{p,L} = Ra_{p,U} = 1000$. If one assumes atmospheric pressure and a reference temperature of $T_{ref} = 17\,^{\circ}\mathrm{C}$, the relevant material properties are: conductivity $k = 0.0263$ W m$^{-1}$ K$^{-1}$, specific heat $c = 1007$ J kg$^{-1}$ K$^{-1}$, thermal diffusivity $\kappa = k/\rho c = 22.5 \times 10^{-6}$ m$^2$ s$^{-1}$, dynamic viscosity $\mu = 184.6 \times 10^{-7}$ N s m$^{-2}$, kinematic viscosity $\nu = 15.89 \times 10^{-6}$ m$^2$ s$^{-1}$, density $\rho = 1.1614$ kg m$^{-3}$, thermal expansion coefficient $\Gamma = 1/(17 + 273) = 1/300$ K$^{-1}$ and gravitational acceleration $g = 9.81$ m s$^{-2}$ (Bergman *et al.* 2011). This leads to $Ra_{p,L} = g\Gamma h^3 T_{p,L}/\nu\kappa = 91.146 \times 10^6 h^3 T_{p,L}$ and a similar expression for $Ra_{p,U}$. If one assumes a permissible temperature difference of $\Delta T = 10\,^{\circ}\mathrm{C}$ ($T_{p,L} = T_{p,U} = 10\,^{\circ}\mathrm{C}$), expressions for the Rayleigh numbers reduce to $Ra_{p,L} = Ra_{p,U} = 911.46 \times 10^6 h^3$. Assuming $Ra_{p,L} = Ra_{p,U} = 200$ leads to $h = 0.006$ m. The same calculation for $Ra_{p,L} = Ra_{p,U} = 500$ leads to $h = 0.0082$ m, and for $Ra_{p,L} = Ra_{p,U} = 1000$ results in $h = 0.0103$. Doubling of the permissible temperature difference to $\Delta T = 20\,^{\circ}\mathrm{C}$ leads to $h = 0.0048$ m for $Ra_{p,L} = Ra_{p,U} = 200$, $h = 0.0065$ m for $Ra_{p,L} = Ra_{p,U} = 500$ and $h = 0.0082$ for $Ra_{p,L} = Ra_{p,U} = 1000$. The present results are thus applicable to channels with heights of a few millimetres. The larger values of the Rayleigh numbers used in this analysis probably enter into the zone where real gas effects begin to play a role but are included in this presentation in order to illustrate the physical trends.

The system performance can be affected by the appearance of secondary flows, especially for the more intense heatings, but its stability characteristics remain to be studied. An analysis of the stability of flows exposed to the one-wall heating demonstrated the appearance of secondary flows in the form of the longitudinal rolls, the transverse rolls and the oblique rolls, depending on the heating wavenumber (Hossain & Floryan 2013*b*, 2015*a*). The appearance of such states results in a significant decrease of the drag reducing effect but the resulting drag can still be lower than the isothermal drag as shown by Floryan & Floryan (2015) in the case of a channel exposed to a combination of periodic and uniform heatings.

## 6. Summary

A pressure-gradient-driven flow in a horizontal channel exposed to thermal modulations has been studied. The upper and lower walls have sinusoidal temperature variations with the same mean values but different amplitudes, and with a phase shift $\Omega$ between them. Detailed results have been presented for fluids with the Prandtl number $Pr = 0.71$.

It has been shown that the intensity of convective effects strongly depends on the phase shift between the upper and lower heating patterns. The most intense convection and the largest drag reduction are achieved when the hot spots are located above each other, and the weakest convection corresponds to the hot and cold spots located above each other. If one uses drag reduction achieved using the single-wall heating as the reference, heating of both walls can increase this drag reduction by a factor of three but only if the proper positioning of both heating patterns is used. Improper positioning can reduce this effect by half.

It has been shown that the drag reduction is associated with the formation of separation bubbles which isolate the main stream from direct contact with the side walls and provide a propulsive power due to the buoyancy-force-driven convection inside of these bubbles. The bubbles form only when the proper heating wavenumber

$\alpha$ is used; the largest drag reduction is achieved for $\alpha \approx 2.5$. A sufficient increase of the Reynolds number $Re$ results in the washing away of the bubbles and this eliminates the drag reducing effect. Heating of both walls with the proper phase shift between the heating patterns doubles the range of Re where this effect remains active. The strength of the drag reducing effect increases proportionally to the second power of the heating intensity (as expressed by the relevant Rayleigh number) but excessive heating results in the convection saturation and reduction of this effect. A detailed analysis of heat fluxes associated with the creation of the heating patterns has been presented. The maximum net heat flow between the walls occurs for $\alpha \approx 1$ and thus does not overlap with the conditions resulting in the largest drag reduction.

**Acknowledgement**

This work has been carried out with the support of NSERC of Canada.

## Appendix A

Definitions of functions used in § 4.

$$\left.\begin{aligned}\theta_{L0} &= -\frac{y}{4}+\frac{1}{4}, \quad \theta_{L2} = -\frac{y^3}{24}+\frac{y^2}{8}+\frac{y}{24}-\frac{1}{8},\\ \theta_{L4} &= -\frac{y^5}{480}+\frac{y^4}{96}+\frac{y^3}{144}-\frac{y^2}{16}-\frac{7y}{1440}+\frac{5}{96},\end{aligned}\right\} \tag{A 1}$$

$$\left.\begin{aligned}\theta_{U0} &= \frac{y}{4}+\frac{1}{4}, \quad \theta_{U2} = \frac{y^3}{24}+\frac{y^2}{8}-\frac{y}{24}-\frac{1}{8},\\ \theta_{U4} &= \frac{y^5}{480}+\frac{y^4}{96}-\frac{y^3}{144}-\frac{y^2}{16}+\frac{7y}{1440}+\frac{5}{96},\end{aligned}\right\} \tag{A 2}$$

$$\left.\begin{aligned}F_{U1}(y) &= \frac{y^4}{96}-\frac{y^3}{24}-\frac{y^2}{80}+\frac{y}{24}+\frac{1}{480},\\ F_{U2}(y) &= -\frac{y^4}{96}-\frac{y^3}{24}+\frac{y^2}{80}+\frac{y}{24}-\frac{1}{480},\end{aligned}\right\} \tag{A 3}$$

$$\left.\begin{aligned}F_{V21}(y) &= -\frac{y^5}{480}+\frac{y^4}{96}+\frac{y^3}{240}-\frac{y^2}{48}-\frac{y}{480}+\frac{1}{96}\\ F_{V22}(y) &= \frac{y^5}{480}+\frac{y^4}{96}-\frac{y^3}{240}-\frac{y^2}{48}+\frac{y}{480}+\frac{1}{96},\end{aligned}\right\} \tag{A 4}$$

$$\left.\begin{aligned}F_{P01}(y) &= -\frac{y^2}{8}+\frac{y}{4}+\frac{1}{40},\\ F_{P02}(y) &= \frac{y^2}{8}+\frac{y}{4}-\frac{1}{40},\end{aligned}\right\} \tag{A 5}$$

$$\left.\begin{aligned}F_{\Theta 11} &= -\frac{y^5}{80}+\frac{y^4}{48}+\frac{y^3}{24}-\frac{y^2}{8}-\frac{7y}{240}+\frac{5}{48},\\ F_{\Theta 12} &= \frac{y^5}{80}+\frac{y^4}{48}-\frac{y^3}{24}-\frac{y^2}{8}+\frac{7y}{240}+\frac{5}{48},\end{aligned}\right\} \tag{A 6}$$

$$F_{U21}(y) = -\frac{y^8}{26\,880} + \frac{y^7}{10\,080} + \frac{y^6}{2880} - \frac{y^5}{480} - \frac{7y^4}{5760} + \frac{5y^3}{288} + \frac{107y^2}{100\,800} - \frac{31y}{2016} - \frac{1}{6400}, \tag{A 7}$$

$$F_{U22}(y) = -\frac{y^8}{8960} + \frac{y^7}{2016} + \frac{7y^6}{14\,400} - \frac{y^5}{480} - \frac{y^4}{1152} + \frac{y^3}{288} + \frac{19y^2}{33\,600} - \frac{19y}{10\,080} - \frac{29}{403\,200}, \tag{A 8}$$

$$F_{U23}(y) = \frac{y^8}{26\,880} + \frac{y^7}{10\,080} - \frac{y^6}{2880} - \frac{y^5}{480} + \frac{7y^4}{5760} + \frac{5y^3}{288} - \frac{107y^2}{100\,800} - \frac{31y}{2016} + \frac{1}{6400}, \tag{A 9}$$

$$F_{U24}(y) = \frac{y^8}{8960} + \frac{y^7}{2016} - \frac{7y^6}{14\,400} - \frac{y^5}{480} + \frac{y^4}{1152} + \frac{y^3}{288} - \frac{19y^2}{33\,600} - \frac{19y}{10\,080} + \frac{29}{403\,200}, \tag{A 10}$$

$$\begin{aligned} F_{V31}(y) \;=\; & -\frac{y^9}{241\,920} + \frac{y^8}{80\,640} + \frac{y^7}{20\,160} - \frac{y^6}{2880} - \frac{7y^5}{28\,800} + \frac{5y^4}{1152} \\ & + \frac{107y^3}{302\,400} - \frac{31y^2}{4032} - \frac{y}{6400} + \frac{33}{8960}, \end{aligned} \tag{A 11}$$

$$\begin{aligned} F_{V32}(y) \;=\; & -\frac{y^9}{80\,640} + \frac{y^8}{16\,128} + \frac{y^7}{14\,400} - \frac{y^6}{2880} - \frac{y^5}{5760} + \frac{y^4}{1152} \\ & + \frac{19y^3}{100\,800} - \frac{19y^2}{20\,160} - \frac{29y}{403\,200} + \frac{29}{80\,640}, \end{aligned} \tag{A 12}$$

$$\begin{aligned} F_{V33}(y) \;=\; & \frac{y^9}{241\,920} + \frac{y^8}{80\,640} - \frac{y^7}{20\,160} - \frac{y^6}{2880} + \frac{7y^5}{28\,800} + \frac{5y^4}{1152} \\ & - \frac{107y^3}{302\,400} - \frac{31y^2}{4032} + \frac{y}{6400} + \frac{33}{8960}, \end{aligned} \tag{A 13}$$

$$\begin{aligned} F_{V34}(y) \;=\; & \frac{y^9}{80\,640} + \frac{y^8}{16\,128} - \frac{y^7}{14\,400} - \frac{y^6}{2880} + \frac{y^5}{5760} + \frac{y^4}{1152} \\ & - \frac{19y^3}{100\,800} - \frac{19y^2}{20\,160} + \frac{29y}{403\,200} + \frac{29}{80\,640}, \end{aligned} \tag{A 14}$$

$$\left.\begin{aligned} F_{P11}(y) &= -\frac{y^6}{480} + \frac{y^5}{240} + \frac{y^4}{96} - \frac{y^3}{24} - \frac{7y^2}{480} + \frac{5y}{48} + \frac{107}{50\,400}, \\ F_{P12}(y) &= \frac{y^6}{480} + \frac{y^5}{240} - \frac{y^4}{96} - \frac{y^3}{24} + \frac{7y^2}{480} + \frac{5y}{48} - \frac{107}{50\,400}, \end{aligned}\right\} \tag{A 15}$$

$$F_{\Theta 21}(y) = \frac{y^7}{26\,880} - \frac{y^6}{3840} + \frac{y^5}{6400} + \frac{y^4}{1280} - \frac{y^3}{1280} - \frac{y^2}{1280} + \frac{79y}{134\,400} + \frac{1}{3840}, \tag{A 16}$$

$$F_{\Theta 22}(y) = -\frac{y^7}{13\,440} + \frac{7y^5}{9600} - \frac{11y^3}{5760} + \frac{253y}{201\,600}, \tag{A 17}$$

$$F_{\Theta 23}(y) = \frac{y^7}{26\,880} + \frac{y^6}{3840} + \frac{y^5}{6400} - \frac{y^4}{1280} - \frac{y^3}{1280} + \frac{y^2}{1280} + \frac{79y}{134\,400} - \frac{1}{3840}, \tag{A 18}$$

$$F_{\Theta 24}(y) = \frac{y^9}{5760} - \frac{y^8}{2688} - \frac{13y^7}{10\,080} + \frac{7y^6}{1440} + \frac{17y^5}{4800} - \frac{11y^4}{576} - \frac{7y^3}{1440} + \frac{5y^2}{96} + \frac{491y}{201\,600} - \frac{1511}{40\,320}, \tag{A 19}$$

$$F_{\Theta 25}(y) = -\frac{y^9}{5760} - \frac{y^8}{2688} + \frac{13y^7}{10\,080} + \frac{7y^6}{1440} - \frac{17y^5}{4800} - \frac{11y^4}{576} + \frac{7y^3}{1440} + \frac{5y^2}{96} - \frac{491y}{201\,600} - \frac{1511}{40\,320}, \tag{A 20}$$

$$F_{\Theta 26}(y) = -\frac{y^7}{40\,320} + \frac{y^6}{5760} - \frac{y^5}{4800} - \frac{y^4}{2880} + \frac{y^3}{1152} - \frac{y^2}{1920} - \frac{y}{1575} + \frac{1}{1440}, \tag{A 21}$$

$$F_{\Theta 27}(y) = \frac{y^7}{20\,160} - \frac{y^5}{1600} + \frac{y^3}{576} - \frac{13y}{11\,200}, \tag{A 22}$$

$$F_{\Theta 28}(y) = -\frac{y^7}{40\,320} - \frac{y^6}{5760} - \frac{y^5}{4800} + \frac{y^4}{2880} + \frac{y^3}{1152} + \frac{y^2}{1920} - \frac{y}{1575} - \frac{1}{1440}. \tag{A 23}$$

## REFERENCES


BERGMAN, T. L., LAVINE, A. S., INCROPERA, F. P. & DEWITT, D. P. 2011 *Fundamentals of Heat and Mass Transfer*, 7th edn. Wiley.

BEWLEY, T. 2009 A fundamental limit on the balance of power in a transpiration-controlled channel flow. *J. Fluid Mech.* **632**, 443–446.

CANUTO, C., HUSSAINI, M. Y., QUARTERONI, A. & ZANG, T. A. 2006 *Spectral Methods: Fundamentals in Single Domains*. Springer.

FLORYAN, J. M. 2012 The thermo-superhydrophobic effect. *Bull. Amer. Phys. Soc.* **57** (1), X.50.00015.

FLORYAN, D. & FLORYAN, J. M. 2015 Drag reduction in heated channels. *J. Fluid Mech.* **765**, 353–395.

FUKAGATA, K., SUGIYAMA, K. & KASAGI, N. 2009 On the lower bound of net driving power in controlled duct flows. *Physica* D **238**, 108–1086.

HŒPFFNER, J. & FUKAGATA, K. 2009 Pumping or drag reduction? *J. Fluid Mech.* **635**, 171–187.

HOSSAIN, M. Z., FLORYAN, D. & FLORYAN, J. M. 2012 Drag reduction due to spatial thermal modulations. *J. Fluid Mech.* **713**, 398–419.

HOSSAIN, M. Z. & FLORYAN, J. M. 2013*a* Heat transfer due to natural convection in a periodically heated slot. *Trans. ASME J. Heat Transfer* **135**, 022503.

HOSSAIN, M. Z. & FLORYAN, J. M. 2013*b* Instabilities of natural convection in a periodically heated layer. *J. Fluid Mech.* **733**, 33–67.

HOSSAIN, M. Z. & FLORYAN, J. M. 2014 Natural convection in a fluid layer periodically heated from above. *Phys. Rev.* E **90**, 023015.

HOSSAIN, M. Z. & FLORYAN, J. M. 2015*a* Mixed convection in a periodically heated channel. *J. Fluid Mech.* **768**, 51–90.

HOSSAIN, M. Z. & FLORYAN, J. M. 2015*b* Natural convection in a horizontal fluid layer periodically heated from above and below. *Phys. Rev.* E **92**, 023015.

HUGHES, G. O. & GRIFFITHS, R. W. 2008 Horizontal convection. *Annu. Rev. Fluid Mech.* **40**, 185–208.

JOSEPH, P., COTTIN-BIZONNE, C., BENOIT, J. M., YBERT, C., JOURNET, C., TABELING, P. & BOCQUET, L. 2006 Slippage of water past superhydrophobic carbon nanotube forests in microchannels. *Phys. Rev. Lett.* **97**, 156104.

MARTIN, S. & BHUSHAN, B. 2014 Fluid flow analysis of a shark-inspired microstructure. *J. Fluid Mech.* **756**, 5–29.

MAXWORTHY, T. 1997 Convection into domains with open boundaries. *Annu. Rev. Fluid. Mech.* **29**, 327–371.

MOHAMMADI, A. & FLORYAN, J. M. 2012 Mechanism of drag generation by surface corrugation. *Phys. Fluids* **24**, 013602.

MOHAMMADI, A. & FLORYAN, J. M. 2013*a* Pressure losses in grooved channels. *J. Fluid Mech.* **725**, 23–54.

MOHAMMADI, A. & FLORYAN, J. M. 2013*b* Groove optimization for drag reduction. *Phys. Fluids* **25**, 113601.

MOHAMMADI, A. & FLORYAN, J. M. 2014 Effects of longitudinal grooves on the Couette–Poiseuille flow. *J. Theor. Comput. Fluid Dyn.* **28**, 549–572.

MOHAMMADI, A. & FLORYAN, J. M. 2015 Numerical analysis of laminar-drag-reducing grooves. *Trans. ASME J. Fluids Engng* **137** (1–12), 041201.

MORADI, H. V. & FLORYAN, J. M. 2013 Flows in annuli with longitudinal grooves. *J. Fluid Mech.* **716**, 280–315.

MORADI, H. V. & FLORYAN, J. M. 2014 Stability of flow in a channel with longitudinal grooves. *J. Fluid Mech.* **757**, 613–648.

OU, J., PEROT, J. B. & ROTHSTEIN, J. P. 2004 Laminar drag reduction in microchannels using ultrahydrophobic surfaces. *Phys. Fluids* **16**, 4635–4643.

OU, J. & ROTHSTEIN, J. P. 2005 Direct velocity measurements of the flow past drag-reducing ultrahydrophobic surfaces. *Phys. Fluids* **17**, 103606.

QUÉRÉ, D. 2008 Wetting and roughness. *Annu. Rev. Mater. Res.* **38**, 71–99.

REYSSAT, M., YEOMANS, J. M. & QUÉRÉ, D. 2008 Impalement of fakir drops. *Europhys. Lett.* **81**, 26006.

ROTHSTEIN, J. P. 2010 Slip on superhydrophobic surfaces. *Annu. Rev. Fluid Mech.* **42**, 89–109.

SAMAHA, M. A., TAFRESHI, H. V. & GAD-EL-HAK, M. 2011 Modeling drag reduction and meniscus stability of superhydrophobic surfaces comprised of random roughness. *Phys. Fluids* **23**, 012001.

SIGGERS, J. H., KERSWELL, R. R. & BALMFORTH, N. J. 2004 Bounds on horizontal convection. *J. Fluid Mech.* **517**, 55–70.

TAKAGI, D. & BALMFORTH, N. J. 2011 Peristaltic pumping of viscous fluid in an elastic tube. *J. Fluid Mech.* **672**, 196–218.

TRUESDELL, R., MAMMOLI, P., VOROBIEFF, P., VAN SWOL, P. & BRINKER, C. J. 2006 Drag reduction on a patterned superhydrophobic surface. *Phys. Rev. Lett.* **97**, 044504.

WINTERS, K. B. & YOUNG, W. R. 2009 Available potential energy and buoyancy variance in horizontal convection. *J. Fluid Mech.* **629**, 221–230.

YAMAMOTO, A., HASEGAWA, Y. & KASAGI, N. 2013 Optimal control of dissimilar heat and momentum transfer in fully developed turbulent channel flow. *J. Fluid Mech.* **733**, 189–230.

ZHOU, M., LI, J., WU, C., ZHOU, X. & CAI, L. 2011 Fluid drag reduction on superhydrophobic surfaces coated with carbon nanotube forest (CNTs). *Soft Matt.* **7**, 4391–4396.